Clim. Past, 11, 449–471, 2015
www.clim-past.net/11/449/2015/
doi:10.5194/cp-11-449-2015

Climate of the Past
Open Access

Global climate simulations at 3000-year intervals for the last 21 000 years with the GENMOM coupled atmosphere–ocean model

J. R. Alder and S. W. Hostetler

US Geological Survey, College of Earth, Ocean and Atmospheric Sciences, Oregon State University, Corvallis, Oregon 97331, USA

Correspondence to: J. R. Alder (jalder@usgs.gov)

Received: 13 June 2014 – Published in Clim. Past Discuss.: 23 July 2014
Revised: 29 January 2015 – Accepted: 12 February 2015 – Published: 17 March 2015

Abstract. We apply GENMOM, a coupled atmosphere–ocean climate model, to simulate eight equilibrium time slices at 3000-year intervals for the past 21 000 years forced by changes in Earth–Sun geometry, atmospheric greenhouse gases (GHGs), continental ice sheets, and sea level. Simulated global cooling during the Last Glacial Maximum (LGM) is 3.8 °C and the rate of post-glacial warming is in overall agreement with recently published temperature reconstructions. The greatest rate of warming occurs between 15 and 12 ka (2.4 °C over land, 0.7 °C over oceans, and 1.4 °C globally) in response to changes in radiative forcing from the diminished extent of the Northern Hemisphere (NH) ice sheets and increases in GHGs and NH summer insolation. The modeled LGM and 6 ka temperature and precipitation climatologies are generally consistent with proxy reconstructions, the PMIP2 and PMIP3 simulations, and other paleoclimate data–model analyses. The model does not capture the mid-Holocene "thermal maximum" and gradual cooling to preindustrial (PI) global temperature found in the data. Simulated monsoonal precipitation in North Africa peaks between 12 and 9 ka at values ∼ 50 % greater than those of the PI, and Indian monsoonal precipitation peaks at 12 and 9 ka at values ∼ 45 % greater than the PI. GENMOM captures the reconstructed LGM extent of NH and Southern Hemisphere (SH) sea ice. The simulated present-day Antarctica Circumpolar Current (ACC) is ∼ 48 % weaker than the observed (62 versus 119 Sv). The simulated present-day Atlantic Meridional Overturning Circulation (AMOC) of 19.3 ± 1.4 Sv on the Bermuda Rise (33° N) is comparable with observed value of 18.7 ± 4.8 Sv. AMOC at 33° N is reduced by ∼ 15 % during the LGM, and the largest post-glacial increase (∼ 11 %) occurs during the 15 ka time slice.

1 Introduction

The history of the climate system over the past 21 000 years reflects the combined changes in Earth–Sun orbital geometry, atmospheric greenhouse gas concentrations (GHGs; see Table A1 for list of abbreviations and acronyms), the extent of the Northern Hemisphere (NH) ice sheets, and sea level. GHG levels were lowest during the Last Glacial Maximum (LGM, ∼ 21 000 years ago, 21 ka) and increased thereafter to preindustrial (PI) levels (Brook et al., 2000; Monnin et al., 2001; Sowers et al., 2003). The LGM is further characterized by the large Laurentide (LIS), Cordilleran (CIS) and Fennoscandian (FIS) ice sheets. The height and extent of the ice sheets altered atmospheric circulation patterns, and the extent increased the NH albedo, thereby altering the global radiative balance. The effect of the ice sheets on climate progressively diminished from the LGM to the early Holocene as global warming driven by increasing GHGs combined with changes in NH summer insolation to accelerate ice sheet ablation. Abrupt departures from the comparatively smooth transition from the LGM through the Holocene, such as Heinrich and Dansgaard–Oeschger events, the Bølling–Allerød (BA), and the Younger Dryas (YD), are evident in geologic records, and these events likely influenced the overall trajectory of the deglaciation.

The climate of the past 21 000 years has been studied extensively, beginning with three international collaborative projects – Climate: Long range Investigation, Mapping, and Prediction (CLIMAP; CLIMAP Project Members, 1981) and the Cooperative Holocene Mapping Project (COHMAP; COHMAP Members, 1988), which evolved into the Testing Earth System Models with Paleoenvironmental Observations (TEMPO) project (Kutzbach et al., 1996a, 1998). CLIMAP

focused on reconstructing the LGM climate; COHMAP focused on reconstructing the climate of seven time periods (18, 15, 12, 9, 6, and 3 ka); and TEMPO focused on reconstructing the climate of 21, 16, 14, 11, and 6 ka. These three projects pioneered data–model comparison through integrating climate model simulations and paleoclimatic data, which motivated the development of new techniques for analyzing geologic data and led to improvements in general circulation models.

More recently, the Paleoclimate Modelling Intercomparison Project (PMIP) is actively working to advance reconstruction of LGM and 6 ka climate through model-to-model evaluations and data–model comparisons. PMIP has now entered the third phase (PMIP3; Braconnot et al., 2012) and is a component of phase 5 of the Climate Model Intercomparison Project (CMIP5). In contrast to CLIMAP, COHMAP, TEMPO, and earlier PMIP model experiments that employed fixed sea surface temperatures (SST) and mixed-layer ocean models, some of the PMIP2 experiments and all of the PMIP3 experiments include fully coupled ocean and atmospheric models. Braconnot et al. (2012) review some of the highlights of the PMIP2 experiments and the design of the PMIP3 experiments and Harrison et al. (2013) evaluate the PMIP3 and PMIP2 simulations of LGM and 6 ka climates with data–model comparisons. In addition, continuous simulations of climate over the last 21 ka have been achieved with Earth system models of intermediate complexity (e.g., Timm and Timmermann, 2007), and the TraCE-21ka project at the National Center for Atmospheric Research (NCAR) conducted continuous, transient climate simulations from 22 to 6.5 ka with the coupled NCAR Community Climate System Model (Liu et al., 2009). Singarayer and Valdes (2010) simulated the climate of the last 120 000 years using model snapshots at 4 and 1 kyr intervals.

Here we explore past changes in late Pleistocene climate using the coupled atmosphere–ocean general circulation model (AOGCM) GENMOM. We simulated multicentury time slices that span the interval from LGM to preindustrial (PI) every 3000 years (21, 18, 15, 12, 9, 6, and 3 ka and PI). The simulations were run with prescribed insolation, GHG concentrations, continental ice sheets, land extent, and sea level as boundary conditions. We analyze the within and between climatology of the time slices and compare the 21 and 6 ka results with terrestrial and marine climate reconstructions and results from the PMIP2 and PMIP3 simulations. The goal of our simulations is to adopt a methodological framework similar to that of PMIP to simulate time slices between the LGM and mid-Holocene. The simulations also serve as a baseline for applying GENMOM to more detailed and focused studies of late Pleistocene climate such as quantifying the effects of freshwater forcing and dynamic vegetation feedbacks.

2 Methods

2.1 Model description

GENMOM combines version 3 of the GENESIS atmospheric model (Pollard and Thompson, 1997; Thompson and Pollard, 1995, 1997) with version 2 of the Modular Ocean Model (MOM2; Pacanowski, 1996). Version 3 of GENESIS (Alder et al., 2011; Kump and Pollard, 2008; Pollard and Thompson, 1997; Zhou et al., 2008) incorporates the NCAR CCM3 radiation code (Kiehl et al., 1998). GENESIS has been developed with an emphasis on representing terrestrial physical and biophysical processes, and for application to paleoclimate experiments. Earlier versions of GENESIS (Pollard and Thompson, 1994, 1995, 1997; Thompson and Pollard, 1995, 1997) have been applied in a wide range of modern and paleoclimate studies (Beckmann et al., 2005; Bice et al., 2006; DeConto et al., 2007, 2008; Horton et al., 2007; Hostetler et al., 2006; Miller et al., 2005; Poulsen et al., 2007a, b; Ruddiman et al., 2005; Tabor et al., 2014), and GENESIS simulations with fixed and slab ocean SSTs were included in PMIP1 (Joussaume et al., 1999; Pinot et al., 1999; Pollard et al., 1998).

In our simulations, we employ a coupled model with T31 spectral truncation, which corresponds to a grid of 96 longitudes (3.75°) by 48 Gaussian latitudes ($\sim 3.71°$). The atmosphere is represented by 18 vertical sigma levels with mid-layers ranging from 0.993 at the surface to 0.005 at the tropopause. GENESIS includes the Land Surface eXchange model, LSX (Pollard and Thompson, 1995), to simulate surface processes and to account for the exchange of energy, mass, and momentum between the land surface and the atmospheric boundary layer. MOM2 has 20 fixed-depth vertical levels and is implemented on essentially the same T31 horizontal grid as GENESIS through cosine-weighted distortion (Pacanowski, 1996). Sea ice is simulated by a three-layer model that accounts for local melting, freezing, and fractional cover (Harvey, 1988; Semtner, 1976) and includes the dynamics associated with wind and ocean current using the cavitating-fluid model of Flato and Hibler (1992). The atmospheric and ocean models interact every 6 h without flux corrections.

GENMOM reproduces observed global circulation patterns, such as the seasonal change in the position and strength of the jetstreams and the major semi-permanent sea level pressure centers (Alder et al., 2011). The simulated present-day (PD) 2 m air temperature climatology (Table 1) is 0.8 °C colder than observations globally, 0.7 °C colder over oceans, and 0.9 °C colder over land. Similar to other AOGCMs (e.g., Lee and Wang, 2014), GENMOM produces a split ITCZ over the equatorial Pacific Ocean.

The preindustrial Atlantic Meridional Overturning Circulation (AMOC) simulated by GENMOM is 19.3 ± 1.4 Sv, which is stronger than, but comparable to, the observed value of 17.4 Sv (Srokosz et al., 2012). Simulated SSTs display a

Table 1. Atmospheric greenhouse gas concentrations for each time slice simulation. The 21 through 3 ka values for CO_2 (Monnin et al., 2001), CH_4 (Brook et al., 2000), and N_2O (Sowers et al., 2003) are estimated from ice core records by averaging the gas concentrations within a $\pm$300-year window centered at the time of interest. For comparison, the PMIP3 concentrations for 6 ka are 280 ppmV and 650 and 270 ppbV for CO_2, CH_4, and N_2O, respectively, and 185 ppmV and 350 and 200 ppbV for 21 ka. In the table, e is eccentricity, ω-180 is precession, and ε is obliquity (Berger and Loutre, 1991).

	CO_2 (ppmV)	CH_4 (ppbV)	N_2O (ppbV)	e	ω-180	ε
PD	355	1714	311	0.0176	101.37	23.446
PI	280	760	270	0.0176	101.37	23.446
3 ka	275	627	264	0.0183	50.30	23.815
6 ka	260	596	227	0.0192	0.01	24.100
9 ka	260	677	244	0.0198	310.32	24.229
12 ka	240	500	246	0.0201	261.07	24.161
15 ka	220	500	216	0.0202	212.04	23.895
18 ka	188	382	219	0.0199	163.04	23.475
21 ka	188	392	199	0.0194	113.98	22.989

warm bias in some regions of the Southern Ocean, primarily south of 50° S around Antarctica, and a warm bias exceeding $\sim$2 °C between 200 and 1000 m depth in parts of the tropics and midlatitudes. Alder et al. (2011) note that the warm bias in the Southern Ocean is associated with the relatively weak Antarctic Circumpolar Current (ACC) in GENMOM (62 Sv versus the observed value of 119 Sv) and Deacon cell upwelling, which allows excessive vertical mixing in the present-day GENMOM simulation, and that these together reduce sea ice around Antarctica, particularly during summer. Both of these features are present to some extent in our suite of simulations. We tested the Gent–McWilliams vertical ocean mixing scheme (Gent and Mcwilliams, 1990) in GENMOM, but it did not improve the Southern Ocean warm bias, so we did not implement it in our paleosimulations.

The climate sensitivity of GENMOM for a doubling of CO_2 from present day is 2.2 °C, which is in the lower range of other coupled AOGCMs (Meehl et al., 2007) and is consistent with recent estimates of 2.7 °C based on the PMIP3 LGM simulations (Harrison et al., 2013) and paleodata–model estimates of 2.8 °C (Annan and Hargreaves, 2013) and 2.3 °C (Schmittner et al., 2011b).

The average NH 2 m temperature in our PI simulation is 0.79 °C cooler than our PD simulation, reflecting lower GHG concentrations, whereas the PD simulation is 1.97 °C cooler than observations and reflects the lower GHG concentrations specified in the PI simulation (Tables 1 and 2). The PI-to-PD warming in the NH is similar to the observed warming of $\sim$0.6–0.9 °C (Brohan et al., 2006) and is in the range of response of other climate models (e.g., Otto-Bliesner et al., 2006b). The greatest regional warming between the PI and PD simulations (not shown) is $\sim$3 °C over the high northern latitudes and northern polar regions during boreal autumn, winter, and spring, consistent with the observed polar amplification (Hassol, 2004).

Table 2. Annual average 2 m air temperatures and precipitation rates for the time slice simulations. NCEP is from the National Center for Environmental Predication NCEP/NCAR Reanalysis data set (Kalnay et al., 1996), PD2X is the 2$\times$ CO_2 simulation, PD is present day, and PI is preindustrial. Parenthetical values are the changes from the previous time slice, e.g., the global average temperature for the PD is 0.77 °C warmer than the PI.

	Temperature (K)			Precipitation (mm d^{-1})		
	Global	Land	Ocean	Global	Land	Ocean
NCEP (1980–2000)	287.52 –	281.66 –	289.84 –	3.09 –	2.30 –	3.40 –
PD2X	288.48 (2.2)	282.06 (2.69)	291.29 (1.91)	3.11 (0.11)	2.17 (0.10)	3.53 (0.13)
PD	286.34 (0.77)	279.37 (0.93)	289.38 (0.70)	3.00 (0.04)	2.07 (0.04)	3.40 (0.05)
PI	285.57 (0.07)	278.44 (−0.03)	288.68 (0.15)	2.95 (0.00)	2.03 (−0.02)	3.36 (0.02)
3 ka	285.50 (0.32)	278.47 (0.30)	288.53 (0.33)	2.95 (0.02)	2.05 (0.00)	3.34 (0.04)
6 ka	285.17 (0.23)	278.18 (0.95)	288.20 (−0.27)	2.93 (0.02)	2.05 (0.00)	3.30 (0.02)
9 ka	284.95 (0.74)	277.23 (1.63)	288.47 (0.22)	2.91 (0.05)	2.05 (0.06)	3.30 (0.03)
12 ka	284.21 (1.40)	275.60 (2.44)	288.25 (0.70)	2.86 (0.09)	1.99 (0.12)	3.26 (0.05)
15 ka	282.81 (0.93)	273.16 (1.53)	287.55 (0.53)	2.77 (0.05)	1.87 (0.09)	3.21 (0.02)
18 ka	281.88 (0.16)	271.63 (0.28)	287.02 (0.06)	2.72 (0.01)	1.78 (0.01)	3.19 (0.01)
21 ka	281.72	271.35	286.96	2.71	1.78	3.18

2.2 Experimental design

We applied GENMOM to eight time periods for 21, 18, 15, 12, 9, 6, 3 ka, and preindustrial. We prescribed insolation at the top of atmosphere for each time slice (Fig. 1) by specifying appropriate orbital parameter values for precession, obliquity, and eccentricity (Table 1; Berger and Loutre, 1991). The solar constant was set to 1367 W m^{-2} for all time periods. We estimated GHG concentrations from ice-core records by applying a $\pm$300-year averaging window centered on the time period of interest (Table 1), and we specified the PMIP3 GHG concentrations for our PI simulation (Braconnot et al., 2007a).

To derive continental ice sheets for the time slices, we used the ICE-4G reconstructions (Peltier, 2002) for the Fennoscandian (FIS) and Cordilleran (CIS) ice sheets and the Oregon State University Laurentide Ice Sheet (OSU-LIS) reconstruction (Hostetler et al., 1999; Licciardi et al., 1998) (Fig. 2). The ICE-6G reconstruction was not available for our eight time slices at the time we began our simulations.

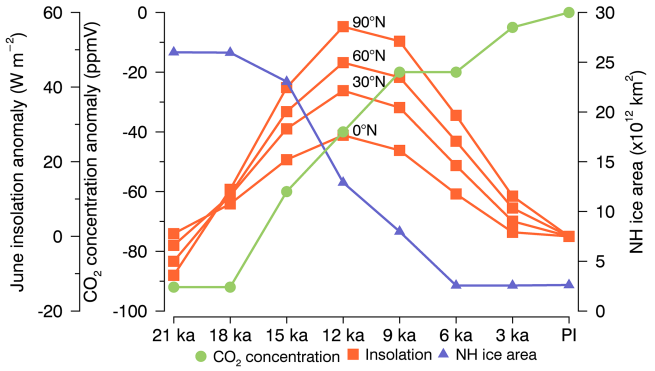

Figure 1. Boundary conditions for the time slice simulations. CO_2 concentrations are relative to the PI concentration of 280 ppmV. NH ice area is the total area covered by the continental ice sheets. June insolation anomalies are relative to PI at the indicated latitude. Mid-month insolation data from Berger and Loutre (1991).

However, the OSU-LIS reconstruction has similar ice sheet topography to that of ICE-6G (Ullman et al., 2014) and was available for our simulation periods. The combination of OSU-LIS and ICE-4G enables us to use a more realistic LIS topography than that of ICE-5G, particularly over the LIS during the deglacial, and facilitates adjusting sea level throughout our time slices. A similar ice sheet configuration (OSU-LIS and ICE-5G) was used as a boundary condition in the NASA GISS-E2-R LGM simulation submitted to the PMIP3 archive (Ullman et al., 2014). We specified the 10 ka OSU-LIS ice sheet to ensure that Hudson Bay remained covered by the LIS at 9 ka (Dyke and Prest, 1987). The ICE-4G reconstruction includes an ice sheet in eastern Siberia, which we removed because it did not exist (Felzer, 2001).

Topographic heights of the land masses were altered to reflect relative sea level change in ICE-4G. We created the topography and land mask for each time slice by applying orographic changes to the present-day Scripps global orography data set (Gates and Nelson, 1975). Orographic changes are based on ICE-4G exposed or flooded land grid cells associated with relative sea level (e.g., Indonesia, Papua New Guinea). We set the ocean bathymetry to modern depths for ocean grid cells.

We specified the modern distribution of vegetation (Dorman and Sellers, 1989) for all simulations because reconstructions of global vegetation for all time slices either do not exist or are not well constrained. We note that while setting vegetation to modern distribution for all simulations isolates the period-to-period climate response to other boundary conditions, we do not capture dynamic vegetation–climate feedbacks that may be important in some regions such as North Africa (Kutzbach et al., 1996b; Timm et al., 2010) and the high latitudes of the NH (Claussen, 2009; Renssen et al., 2004). The vegetation type on emergent land cells is set to be the same as neighboring existing land cells. The simulations do not include varying dust forcing across the time slices, which may account for up to 20 % of the radiative change (Köhler et al., 2010; Rohling et al., 2012). Freshwater flux from land-based precipitation is globally averaged and spread over the world ocean (Alder et al., 2011).

In accordance with the PMIP3 protocol, to conserve atmospheric mass we compensated for changes in global topography in each time slice by holding global average surface pressure constant. At T31 resolution the Bering Strait and the Strait of Gibraltar are closed in the default MOM2 bathymetry. We conducted sensitivity tests and adjusted the bathymetry to ensure that key passages (e.g., Drake Passage, Norwegian Sea, and Indonesian Throughflow) were adequately represented. Additional sensitivity testing revealed that the modeled AMOC and salinity of the Arctic are very sensitive to the bathymetry of the Norwegian Sea, particularly to the width of the passage between Scandinavia and Greenland as it narrowed by the growth of the FIS. We removed Iceland from the model to ensure that the passage remained sufficiently wide and deep to prevent unrealistic buildup of salinity in the Arctic.

Each time slice simulation was initialized from a cold start (isothermal atmosphere, latitudinally dependent ocean temperature profile, and uniform salinity of 35 ppt) and run for 1100 years. We exclude the first 1000 years from our analysis here to allow for spinup of ocean temperatures. The temperature drift in the last 300 years of our simulations (Fig. S1 in the Supplement) is acceptably small (Braconnot et al., 2007a; Singarayer and Valdes, 2010), with values of -0.05 °C per century for the LGM, 0.01 °C per century for 6 ka, and -0.02 °C per century for PI. Drift in the LGM and early deglacial simulation is attributed primarily to long-term cooling and the evolution of sea ice in the southern ocean. Simulated AMOC exhibits decadal-scale variability, but was free of drift over the last 300 years of the simulations.

In what follows, the monthly averages of the model output are based on the modern calendar as opposed to the angular calendar that changes with Earth–Sun geometry (Pollard and Reusch, 2002; Timm et al., 2008). The modern calendar is commonly used in data–model comparisons (e.g., Harrison, 2013).

3 Results

3.1 Atmospheric circulation

The boreal winter (DFJ) 500 hPa heights in the PI simulation (Fig. 3a) display the observed high- and midlatitude ridge–trough–ridge–trough standing wave structure (wave number two) that arises from continent–ocean–continent–ocean geography of the NH (Peixoto and Oort, 1992). From 21 to 9 ka the LIS, the FIS, and Greenland Ice Sheet alter the NH standing wave structure, resulting in persistent, distinct troughs and cyclonic flow tendencies over northeastern Asia, the North Pacific, the continental interior of North America,

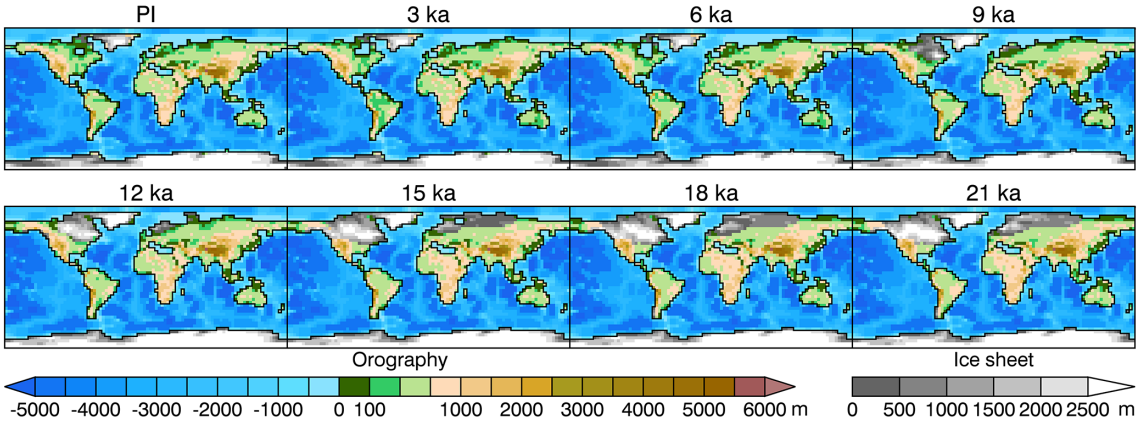

Figure 2. Orography for the time slice simulations, with ice sheet height and extent derived from ICE-4G (Peltier, 2002) for the Fennoscandian, Cordilleran, and Antarctic, and OSU-LIS (Licciardi et al., 1998) for the Laurentide.

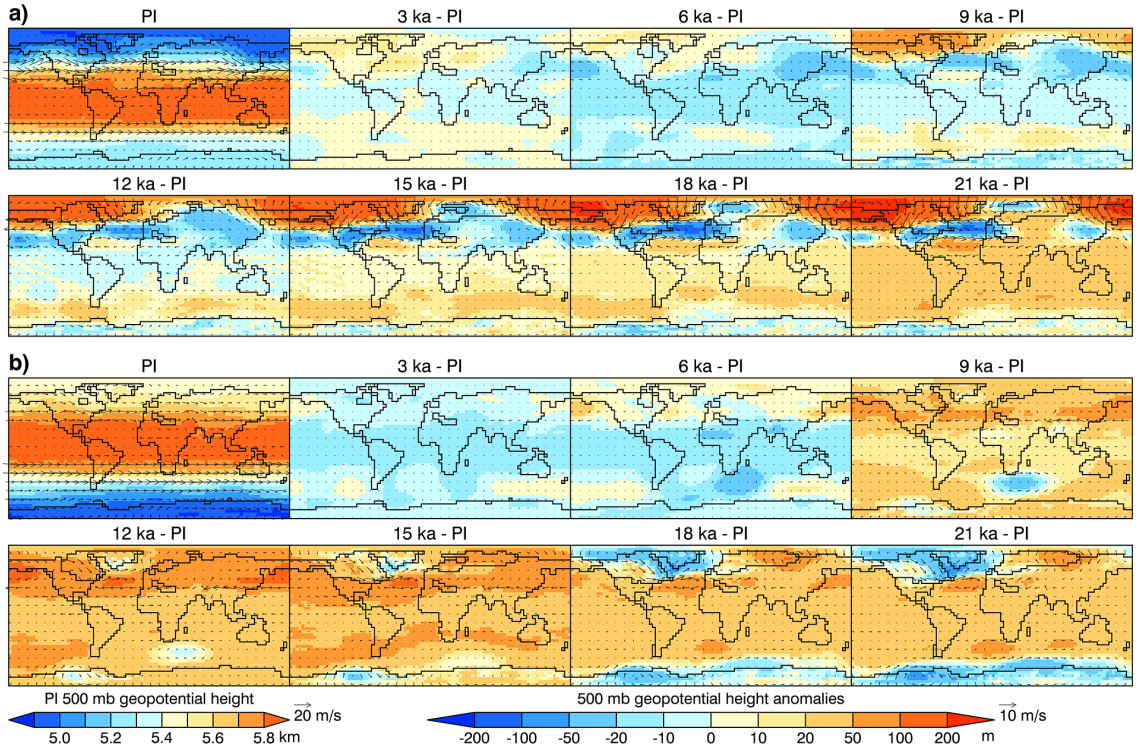

Figure 3. Simulated seasonal 500 hPa geopotential height and wind anomalies relative to PI. **(a)** December, January, and February and **(b)** June, July, and August. Raw 500 hPa geopotential height and wind are shown in Fig. S2 in the Supplement.

the North Atlantic, and Europe (Fig. 3; maps of raw fields, Fig. S2).

Consistent with previous LGM studies using comparable (Braconnot et al., 2007a) and higher-resolution (Kim et al., 2007; Unterman et al., 2011) climate models, from 21 through 9 ka, the western edge of the Cordilleran Ice Sheet diverts the LGM winter polar jetstream, resulting in one branch that is weaker than PI over the Gulf of Alaska and the western and central regions of the ice sheet and a second branch to the south of the ice sheet that is stronger than the PI (Fig. 3a). The reorganization creates westward wind anomalies over the North American Pacific Northwest. The LIS effectively guides the convergence of the branches, and the meridional gradient of low and high 500 hPa height anomalies in the North Atlantic intensifies flow over North America, the North Atlantic, Europe, and North Africa (Figs. 3a), thereby altering the path of storm tracks. This flow pattern weakens progressively as the LIS recedes.

The influence of the NH ice sheets is also evident in summer (JJA), but to a lesser degree than in winter (Fig. 3b)

due to continental heating and the absence of the strong, midlatitude storm tracks. Between 21 and 15 ka, the summer jetstream is constrained and therefore enhanced along and to the south of the southern margin of the LIS extending over the North Atlantic. At 18 ka, a trend toward positive JJA anomalies in 500 hPa heights emerges over the regions of the semi-permanent subtropical high pressure of the North Pacific and central Atlantic. The regions of positive height anomalies, and their associated anticyclonic wind anomalies, expand over central North America, peak from 12 through 9 ka, and diminish by 6 ka (Fig. 3). The DJF pattern of low-to-high height anomalies over the North Atlantic is replaced during JJA by a strengthened subtropical high. Anticyclonic flow around positive height anomalies on the western edge of the FIS alters regional flow patterns over and south of the ice sheet. The GENMOM responses to the NH ice sheets are similar to many previous modeling experiments that have established that changes in tropospheric pressure–surface heights and winds are primarily driven by changes in ice sheet height, and secondarily by temperature and albedo feedbacks (COHMAP Members, 1988; Felzer et al., 1996; 1998; Otto-Bliesner et al., 2006a; Pausata et al., 2011; Pollard and Thompson, 1997; Rind, 1987).

From 21 to 12 ka, the largest changes in boreal winter sea level pressure (SLP) are associated with negative surface temperature anomalies over the continental ice sheets, the landmasses of the NH, and areas of expanded sea ice in the North Atlantic (Fig. 4a) where cooling increases subsidence and thus contributes to cold high surface pressure. From 21 to 15 ka, high pressure over the LIS produces anticyclonic flow across the northern Great Plains and over the Puget Lowland of the US. Similar anticyclonic tendencies are simulated along the margin of the FIS. Between 12 and 6 ka the winter SLP around the Aleutian low in the North Pacific and the Icelandic low in the North Atlantic is strengthened relative to PI. The Aleutian low is expanded southward, whereas the Icelandic low is confined on the northern edge by the FIS and is slightly displaced southeastward.

From 21 to 9 ka, the JJA SLP anomalies remain strongly positive over the ice sheets and sea ice, whereas from 12 to 6 ka the SLP anomalies over Northern Hemisphere landmasses are negative due to enhanced continental warming (Fig. 4b). The patterns of the JJA 500 hPa heights, SLP and the associated circulation over North America and adjacent oceans again illustrate similar responses to time-varying controls: changes from 21 to 15 ka are primarily driven by changes in the LIS, whereas from 12 to 6 ka the circulation changes are related to the changes in the seasonality of Holocene NH insolation (Fig. 2).

3.2 Near-surface air temperature

Our time slice simulations clearly display surface air temperature (SAT) changes attributed to radiative forcing from the presence of the continental ice sheets, GHGs (Clark et al., 2012), and insolation (Fig. 5). The global average mean annual LGM temperature simulated by GENMOM is 3.8 °C colder than the PI (Table 2, Fig. 5a), within the range of cooling in the PMIP2 AOGCM simulations (3.1–5.6 °C and average 4.4 °C) and the PMIP3 simulations (2.6–5.0 °C and average of 4.4 °C) that were forced by similar boundary conditions (Harrison et al., 2013; Kageyama et al., 2006). Our LGM cooling is also in agreement with Annan and Hargreaves (2013), who reconciled the PMIP2 ensemble and proxy data to derive an estimated cooling of 4.0 ± 0.8 °C, but falls outside the range of Schmittner et al. (2011b), who found a median cooling of 3.0 °C (66 % probability range of 2.1–3.3 °C). GENMOM is also consistent with three transient simulations (Liu et al., 2014) averaged over the periods simulated by GENMOM. With the BA and YD excluded, our simulations reproduce the rate of warming between 21 and 15 ka, but they are consistently ~ 1 °C colder than the reconstruction of Shakun et al. (2012) when sampled at the proxy sites (Fig. 5b). During these periods, GENMOM falls at the low end or outside the range of the transient models; however, GENMOM falls within the range of LGM and mid-Holocene cooling simulated by the PMIP3 models, which have similar experimental designs and large-scale boundary conditions.

Neither GENMOM nor the ensemble mean of the PMIP3 models captures the ~ 0.5 °C the 6 ka temperature anomaly in the Marcott et al. (2013) reconstruction. The change in the 6 ka mean annual temperature at the proxy sites in the 12 PMIP3 models we analyzed ranged from -0.3 to 0.3 °C with a mean of ~ 0.0 °C. Three models simulated slight warming, five near zero and four simulated slight cooling. Whether or not some proxies used in the temperature reconstructions have seasonal bias, which would exaggerate the mid-Holocene warming, remains an open research question (Liu et al., 2014).

Seasonal temperature changes across our time slice simulations illustrate the spatial and temporal effect of changing boundary conditions (Fig. 6). From 21 through 15 ka, both DJF and JJA exhibit cold temperature anomalies exceeding 16 °C over and adjacent to the ice sheets in both hemispheres. With the exception of Europe and the high latitudes of the NH, boreal winters remain generally colder than PI over the continents until 3 ka (Fig. 6), corresponding to reduced insolation. NH atmospheric circulation changes induced by atmospheric blocking from the LIS (Fig. 3) sustain positive winter and summer temperature anomalies over Beringia. Summer warming also occurs south of the FIS across much of Asia. Although the mid-Holocene wintertime deficit in insolation is small at high northern latitudes, changes in shortwave radiation at the surface during boreal summer in the model are large and positive (30–40 Wm^{-2}) due to the precessional shift of perihelion and changes in obliquity (Fig. S4). Substantial warming occurs between most pairs of consecutive time slices from the LGM through the Holocene (Fig. 7, Table 2); however, over the African

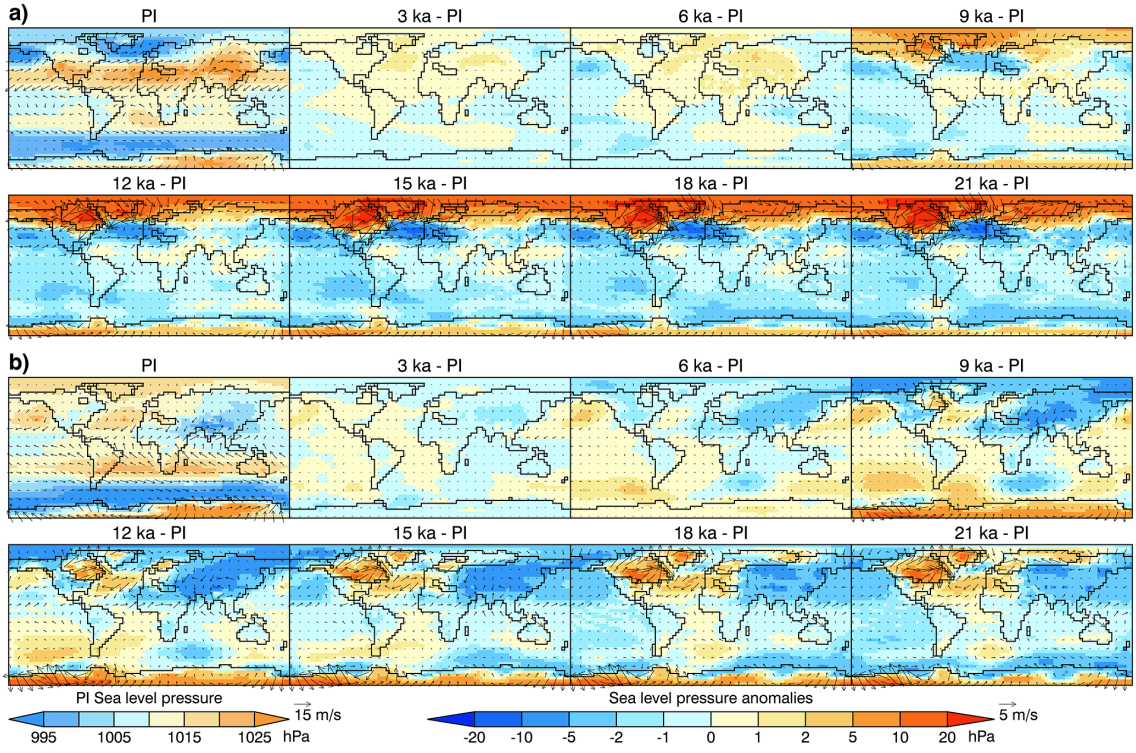

Figure 4. Simulated seasonal average sea level pressure and 2 m wind anomalies relative to PI. **(a)** December, January, and February and **(b)** June, July, and August. Raw sea level pressure and wind are shown in Fig. S3.

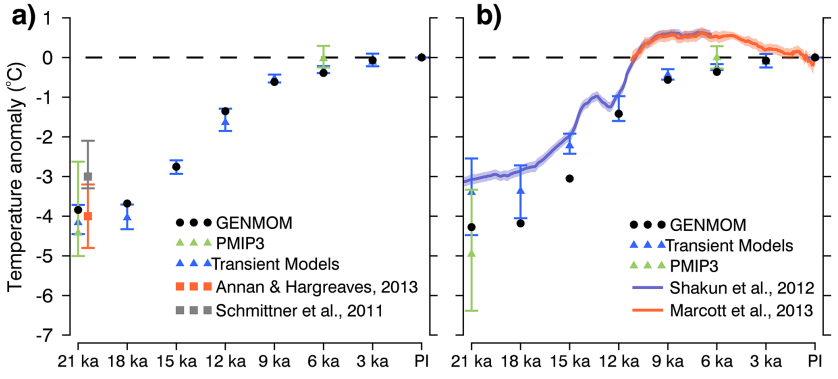

Figure 5. Simulated and reconstructed changes in temperature from 21 ka to present. **(a)** Global mean surface air temperature from GENMOM compared to the PMIP3 ensemble average and three transient models (CCSM – Liu et al., 2009; LOVECLIM – Timm and Timmermann, 2007; and FAMOUS – Smith and Gregory, 2012). The transient model values are averages over a ±50-year window centered on the eight time slices. The symbols for the PMIP and transient models are the average of the ensembles and the bars represent the range of the ensembles. Data-model estimates of mean and range of LGM cooling by Annan and Hargreaves (2013) and Schmittner et al. (2011b) are offset from 21 ka for legibility. **(b)** Temperature change at the proxy sites used in the reconstructions by Shakun et al. (2012) and Marcott et al. (2013). The models were bilinearly interpolated and aggregated to the $5° \times 5°$ boxes around the proxy sites as in Marcott et al. (2013). The 1σ uncertainty in the reconstructions is indicated by the shaded band. Marcott et al. (2013) is adjusted to a preindustrial ($\sim$ 1850) base value rather than the original 1961–1990. Data younger than preindustrial are removed. The Shakun et al. (2012) and Marcott et al. (2013) time series are joined at their 11.5–6.5 ka means.

and Indian monsoon regions, increased cloudiness associated with enhanced summer monsoonal precipitation leads to cooling from 15 to 6 ka.

The relatively high rate of warming between 18 and 15 ka (1.5 °C land and 0.5 °C ocean, Fig. 7, Table 2) is commensurate with increased GHGs (Table 1). Periods of peak annual warming from 15 to 12 ka (2.4 °C land and 0.7 °C ocean) and

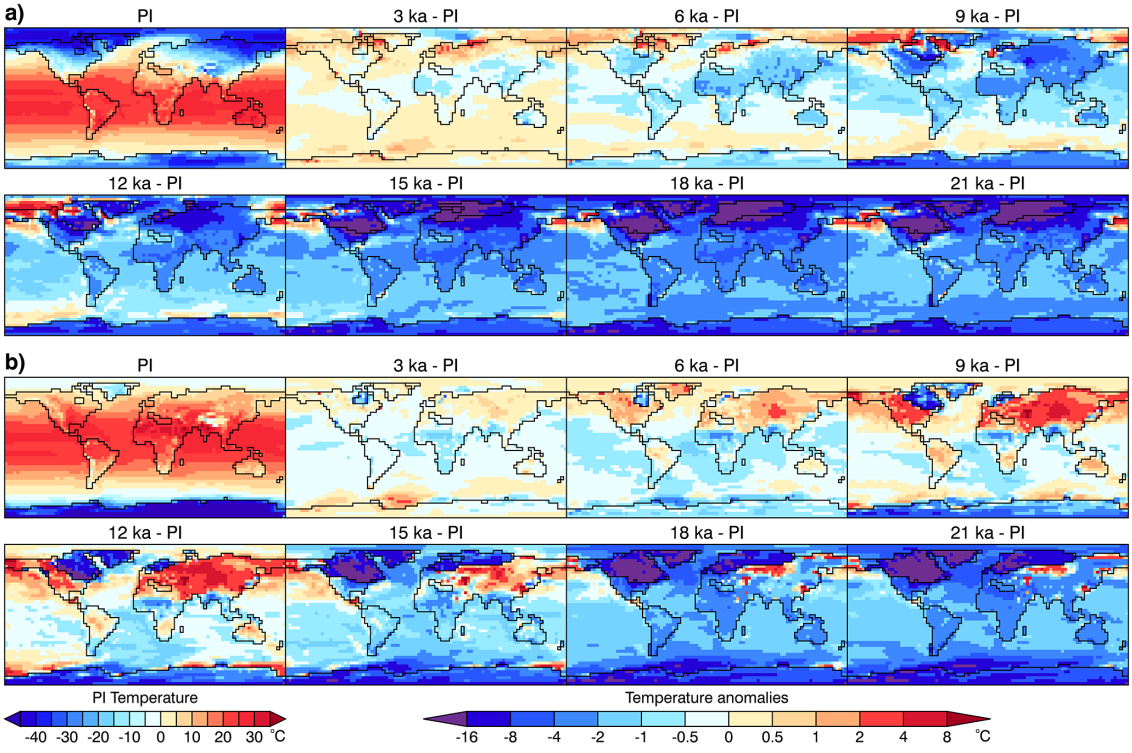

Figure 6. Simulated seasonal average 2 m air temperature anomalies relative to PI. **(a)** December, January, and February and **(b)** June, July, and August.

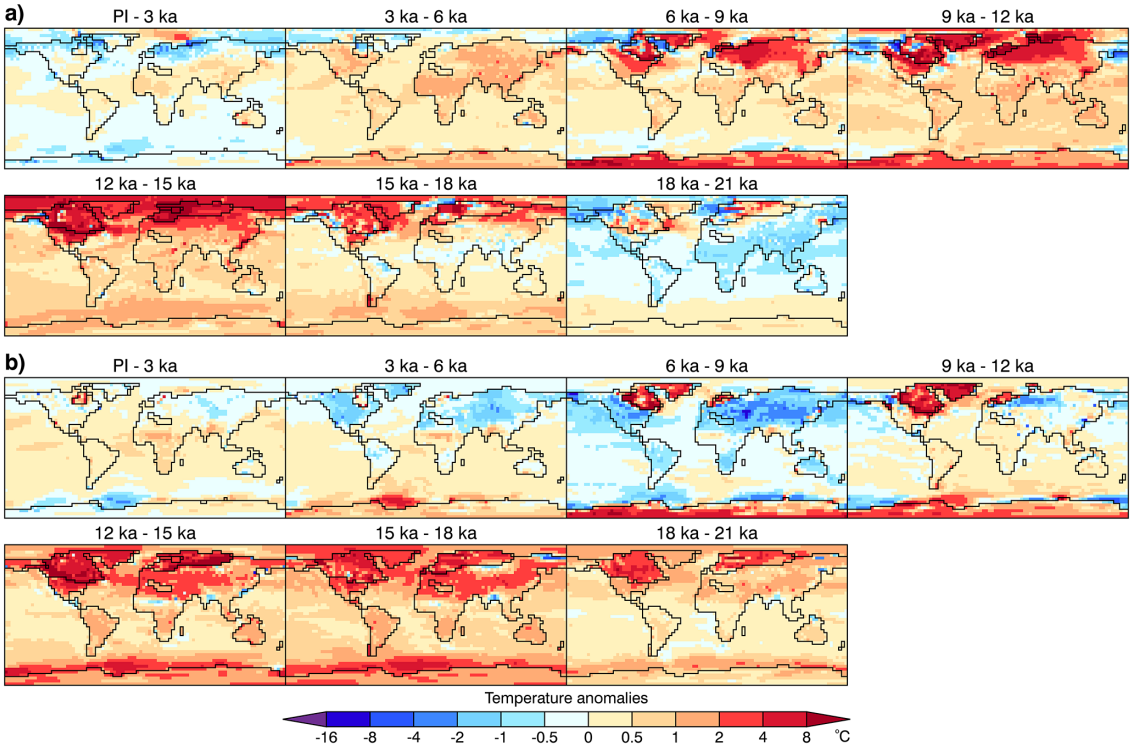

Figure 7. Simulated seasonal average changes in 2 m air between consecutive time slices. **(a)** December, January, and February and **(b)** June, July, and August.

from 12 to 9 ka (1.6 °C land and 0.2 °C ocean) are associated with increasing GHG concentrations and ablation of the NH ice sheets (Figs. 1 and 6a). The simulated rates of annual global warming between the LGM and the early Holocene (Fig. 5) are in agreement with data (Clark et al., 2012; Gasse, 2000) and the analyses by Shakun et al. (2012) and Marcott et al. (2013), who attribute a large component of the warming to rising GHG levels.

The DJF and JJA temperature differences in our 21 ka simulation are similar to those of the PMIP3, allowing for differences in between our prescribed NH ice sheets (ICE-4G+OSU-LIS in GENMOM) and the blended ice sheet of the PMIP3 simulations that essentially combines the height of the ICE-6G reconstruction with the extent of the Dyke and Prest (1987) reconstructions (Figs. S5–S10; Braconnot et al., 2012). In both seasons, GENMOM produces 0.5–1 °C less cooling in the tropical oceans and greater warming over Beringia. The positive JJA temperature anomaly south of the FIS in GENMOM persists through 15 ka. Summer warming in the presence of the ice sheet was identified in earlier versions of GENESIS (Pollard and Thompson, 1997) and is associated with subsidence over the ice (Rind, 1987). Similar JJA warming also occurs in some of the PMIP3 models, but is likely a model artifact (Pollard and Thompson, 1997; Ramstein and Joussaume, 1995; Rind, 1987).

The DJF and JJA temperature anomalies in our 6 ka simulation are also similar to those of the PMIP3 models (Figs. S7 and S8). Relative to PI, GENMOM produces slightly greater winter warming over Scandinavia than is evident in the average of the PMIP3 simulations, and is generally 0.5–1.0 °C cooler over Asia, Africa, and South America. During boreal summer, GENMOM simulates warming over the NH landmasses and cooling over the North African and Indian monsoon regions, consistent with the PMIP3 models. Continental warming in GENMOM is ∼ 0.5–1.0 °C weaker than most PMIP3 models, particularly in Europe and Asia. A portion of the weaker warming in GENMOM is attributed to the prescribed 6 ka GHG concentrations we derived from the ice-core data, which differ slightly from those specified for the PMIP3 experiments (Table 1 caption).

3.3 Precipitation and monsoons

The simulated global precipitation anomalies display a progression from the drier and colder conditions of the LGM to the warmer and wetter conditions of the Holocene (Fig. 8, Table 2). The global mean annual precipitation change of $-0.29\,\mathrm{mm\,d^{-1}}$ for the LGM is distributed as greater drying over land and ice sheets ($-0.30\,\mathrm{mm\,d^{-1}}$) than oceans ($-0.22\,\mathrm{mm\,d^{-1}}$). Regionally coherent patterns of precipitation change (Figs. 8 and 9) are indicative of displacement and changes in the strength of storm tracks (Li and Battisti, 2008), the ITCZ, and the Hadley circulation, as well as the onset, amplification, and subsequent weakening of the global monsoons regions (Broccoli et al., 2006; Chiang, 2009; Chiang and Bitz, 2005).

Between the LGM and 15 ka, during DJF, areas over and adjacent to the NH ice sheets display predominately reduced precipitation arising from a combination of the desertification effect of the high and cold ice; lower-than-present atmospheric moisture; and cloudiness and the advection of cold, dry air off of the ice sheets (Figs. 3a, 4a, 6a, and 8a). The topographic and thermal effects of the LIS and the thermal effect of sea ice (Kageyama et al., 1999; Li and Battisti, 2008) alter 500 hPa geopotential heights along the southern margin of the ice sheet (Figs. 3a and S2a), causing the development of positive precipitation anomalies extending from the eastern Pacific across the Gulf of Mexico and eastern North America and into the North Atlantic. Accompanying negative precipitation anomalies over the North Atlantic and positive anomalies over the Nordic Seas are related to changes in the location of storm tracks. The local effect of the ice sheets on precipitation diminishes during the early and mid-Holocene as their influence on circulation weakens and the atmosphere becomes warmer and moister (Fig. 9a).

The negative DJF anomalies that persist from 21 to 15 ka during austral summer along the equatorial and low-latitude areas of South and Central America, south-central Africa, Southeast Asia, northern Australia, the tropical Atlantic, the Indian Ocean, and the western Pacific warm pool are caused by changes in the location of the ITCZ and weakened southern monsoonal circulation. This particularly affects the winter monsoon in central South America (Cheng et al., 2012; Zhao and Harrison, 2012) and in Southeast Asia and Indonesia, where additional feedbacks in the energy and water balances over emergent land areas occur during low sea level stands (Figs. 1 and 8a) have been shown to alter the Walker Circulation (DiNezio and Tierney, 2013).

Precipitation for JJA also exhibits considerable change over time (Figs. 8b and 9b). Similar to DJF, generally drier conditions are simulated over and adjacent to the NH ice sheets where anticyclonic flow tendencies suppress precipitation (Fig. 4b). Along portions of the southern margins of the LIS and FIS, however, orographic lifting enhances precipitation at 21 ka (Pollard and Thompson, 1997). Wetter conditions in the North American Southwest derive from enhanced westerly flow aloft and lower level southwesterly flow off the eastern Pacific that are associated with displacement of the jetstream by the ice sheets and the weakened Pacific subtropical high. Between 21 and 12 ka the LIS causes an increased pressure gradient from a strengthened Azores–Bermuda High and weakened subtropical high in the eastern Pacific (Figs. 3b and 4b), resulting in amplified and displaced westward winds, drying over Central America, and wetter-than-present conditions over northern South America. At the LGM, North Africa, Europe, and all but the western edge of Asia are drier than the PI, again reflecting the drier atmosphere of the full glacial.

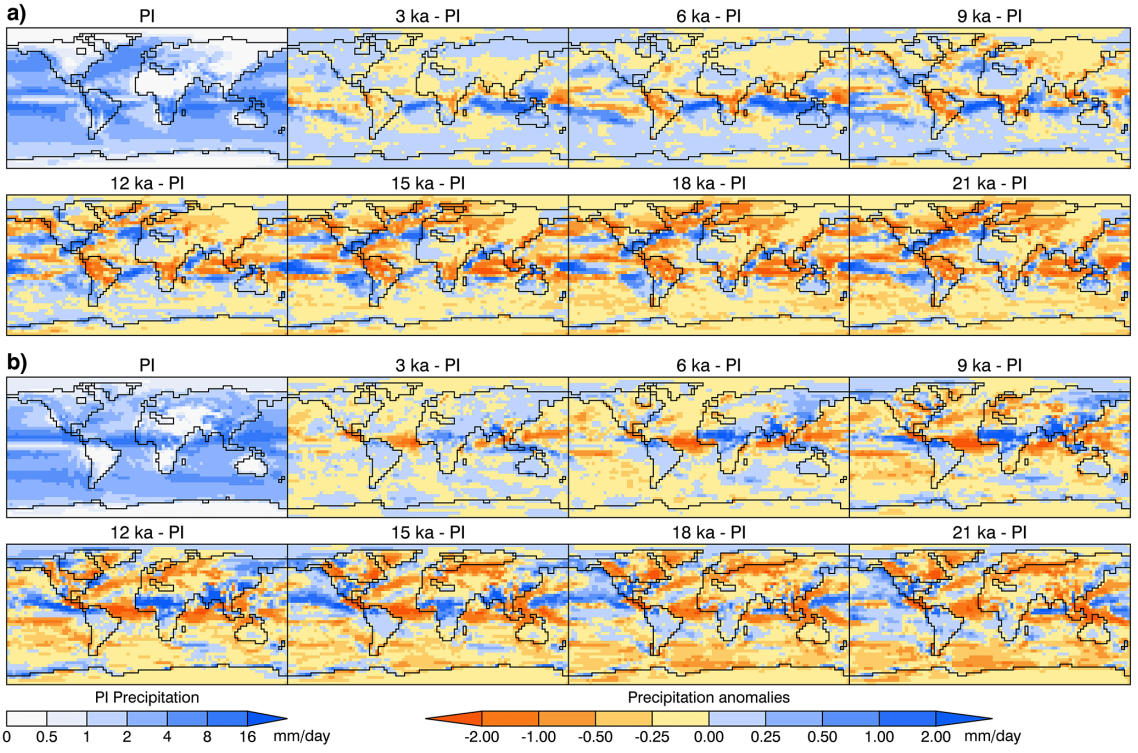

Figure 8. Simulated seasonal average precipitation anomalies relative to PI. **(a)** December, January, and February and **(b)** June, July, and August.

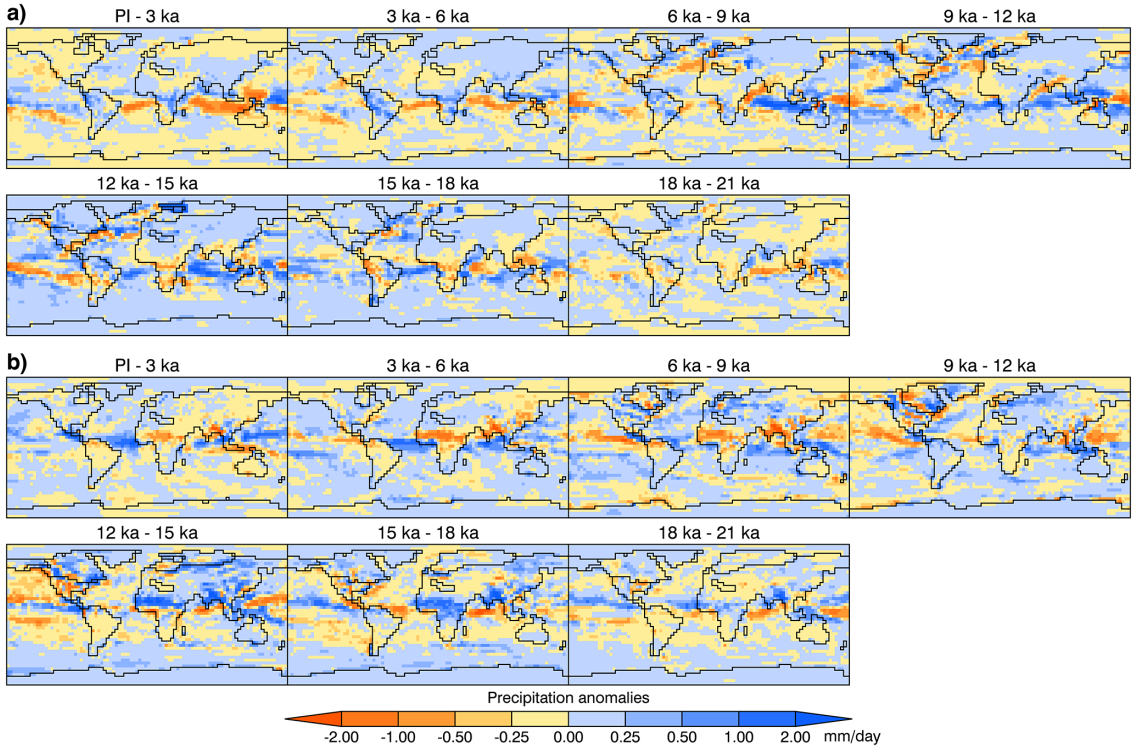

Figure 9. Simulated seasonal average precipitation changes between consecutive time slices. **(a)** December, January, and February and **(b)** June, July, and August.

The magnitude, gradients, and spatial patterns of GENMOM 21 ka DJF precipitation anomalies are consistent with the PMIP3 experiments. Notable exceptions are greater drying than some models in the North Atlantic and the band of positive anomalies extending across the Gulf of Mexico and the southeastern USA. GENMOM produces positive precipitation anomalies over Australia, which is present in four of the PMIP3 models. The 21 ka JJA precipitation anomalies are also in agreement with PMIP3, but display weaker drying over eastern NA and slight drying over the North African monsoon region.

The time evolution from LGM to PI of the African and Indian monsoons reflects the interplay of changes in the location of the ITCZ and Hadley circulation that are linked to the receding NH ice sheets, GHG-driven global warming, enhanced NH JJA insolation, and changing land–SST temperature contrast. The North African and Indian monsoons are suppressed between 21 and 18 ka. After 18 ka, wetter-than-present conditions emerge in the monsoon regions of North Africa and India, where increased JJA insolation warms the continents, which amplifies the land–sea temperature contrasts that drive monsoonal circulation (Braconnot et al., 2007b; Kutzbach and Otto-Bliesner, 1982; Zhao and Harrison, 2012). The simulated DJF air temperatures in North Africa cool from the LGM until 15 ka, and then warm monotonically through the rest of the deglaciation and Holocene (Fig. 10). Wintertime precipitation over the North African region is minimal. In contrast, JJA temperatures increase throughout the deglaciation, peak at 9 ka, decrease slightly at 6 ka, and increase thereafter. A commensurate increase in JJA precipitation over North Africa between 12 and 6 ka is associated with northward migration of the ITCZ (Braconnot et al., 2007a, b; Kutzbach and Liu, 1997), which enhances the transport of moisture into both the North African and Indian monsoon regions. Monsoonal precipitation peaks over both regions between 12 and 9 ka (Fig. 10). The change in precipitation between 9 and 6 ka over India ($0.9\,\mathrm{mm\,d^{-1}}$) is nearly double the change over North Africa ($0.5\,\mathrm{mm\,d^{-1}}$), consistent with the diagnoses of the mid-Holocene monsoon of Marzin and Braconnot (2009), who attribute the stronger ∼ 9 ka monsoon to insolation related to precession and snow cover on the Tibetan Plateau. The pattern of precipitation in the Indian monsoon region is similar to that of North Africa but exhibits a greater range between peak Holocene values and the PI.

The overall temporal progression and magnitude of precipitation changes in the time slice simulations are in agreement with the PMIP2 (Braconnot et al., 2007a, b) and PMIP3 simulations at 21 and 6 ka, and with other mid-Holocene modeling studies (Hély et al., 2009; Kutzbach and Liu, 1997; Kutzbach and Otto-Bliesner, 1982; Timm et al., 2010). More specifically, the June through September GENMOM precipitation anomaly of $-0.6\,\mathrm{mm\,d^{-1}}$ over the North African monsoon region during the LGM is within the range (-0.9 to $0.1\,\mathrm{mm\,d^{-1}}$) of five PMIP2 AOGCMs (Braconnot et al., 2007a) and seven PMIP3 models (range of -0.6 to 0.2 and average of $-0.2\,\mathrm{mm\,d^{-1}}$). The GENMOM LGM anomaly over India ($-0.9\,\mathrm{mm\,d^{-1}}$) is also within the range (-1.7 to $-0.1\,\mathrm{mm\,d^{-1}}$) of the PMIP2 simulations (Braconnot et al., 2007a) and the PMIP3 simulations (range of -1.3 to 0.0 and average of $-0.7\,\mathrm{mm\,d^{-1}}$).

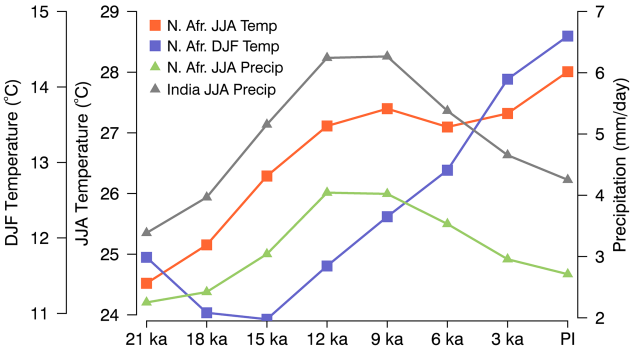

Figure 10. Time evolution of North African and Indian summer monsoons. The North African monsoon region is defined as 12–30° N, 20° W–30° E and Indian monsoon region is defined as 20–40° N, 70–100° E (Zhao and Harrison, 2012).

The northward expansion and spatial pattern of precipitation anomalies of the 6 ka monsoons are in very good agreement with both the PMIP2 and PMIP3 experiments. Summer precipitation in the GENMOM simulation is enhanced by $0.9\,\mathrm{mm\,d^{-1}}$ relative to PI over North Africa, in agreement with the range (0.2–$1.4\,\mathrm{mm\,d^{-1}}$) and mean ($0.7\,\mathrm{mm\,d^{-1}}$) of 11 PMIP2 AOGCMs (Zhao and Harrison, 2012) and 12 PMIP3 models (range of 0.1–1.0 and average of $0.6\,\mathrm{mm\,d^{-1}}$). Over India, the 6 ka GENMOM precipitation anomaly of $1.1\,\mathrm{mm\,d^{-1}}$ exceeds the range (0.2–0.9 $\mathrm{mmd^{-1}}$) and mean ($0.6\,\mathrm{mm\,d^{-1}}$) of the 11 PMIP2 models (Zhao and Harrison, 2012), but is within the range of the PMIP3 models (0.5–1.3 and average of $1.0\,\mathrm{mm\,d^{-1}}$).

3.4 Sea ice

DJF sea ice is present in the PI simulation over Hudson Bay and the Arctic Ocean; along the coast of eastern Canada; and around Greenland, the Nordic Seas, and the Baltic and North seas (Fig. 11), in agreement with observed present-day distributions (Jaccard et al., 2005). Ice fractions of up to 100 % are simulated over the Bering Sea and the Sea of Okhotsk. In the SH, sea ice persists through austral summer in the Weddell and Ross seas and a few scattered locations around Antarctica. While the locations of the ice around Antarctica are in agreement with observations (Gersonde et al., 2005), the model underestimates the ice extent over the Weddell Sea and between the Weddell and Ross seas. The lack of ice is partly attributable to a warm bias in the Southern Ocean associated with the previously mentioned weak ACC (discussed further below). During August and September, simulated sea ice is greatly reduced in the North Atlantic region

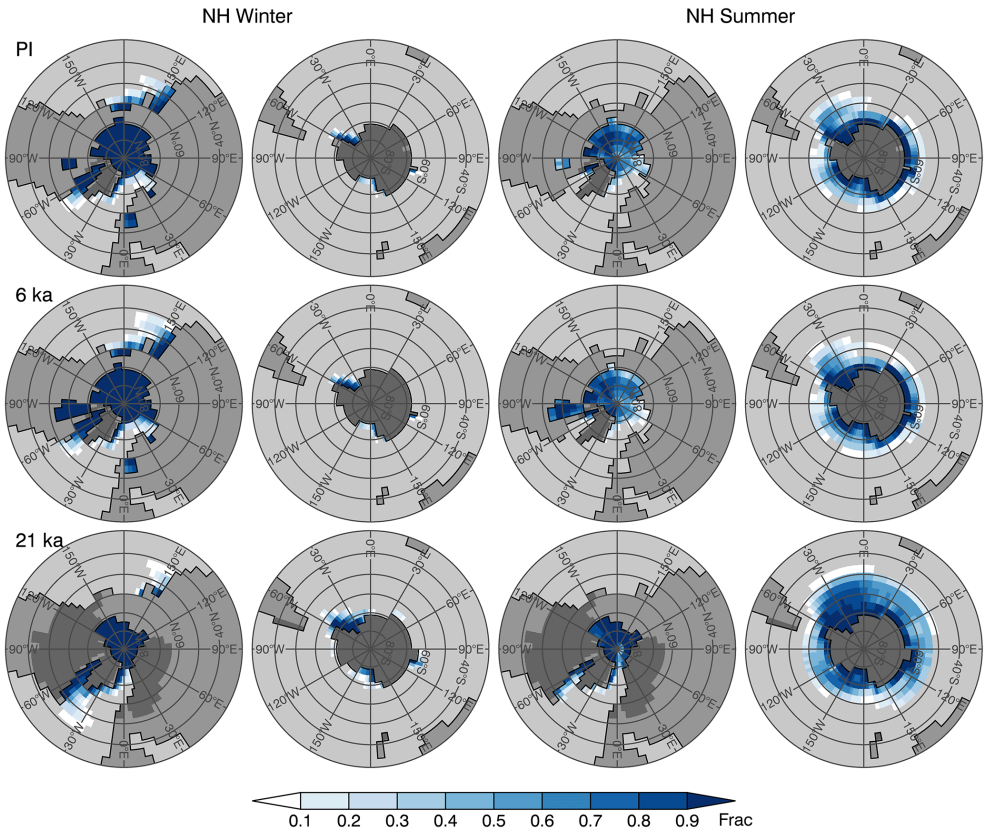

Figure 11. Simulated sea ice fraction for PI and 6 and 21 ka. Left two columns: February–March. Right two columns: August–September. Medium gray is continental land mass and dark gray is continental ice sheet.

(Fig. 11), with remnant ice persisting in the extreme north of Baffin Bay, and the east coast of Greenland, also in agreement with observations. In the SH, the corresponding winter sea ice grows substantially and the distribution is in generally good agreement with observations (Gersonde et al., 2005).

The simulated annual average ice extents for the NH are 9.8×10^6 km^2 for the LGM, 15.8×10^6 km^2 for 6 ka, and 14.1×10^6 km^2 for PI (grid cells with fractional coverage > 15 %). Compounded with climate forcing, changes in both the distribution and areal coverage of the NH ice also reflect the change in ocean area due to the transition of land and ice sheets to ocean as sea level rises (Figs. 11 and S13–S15). For the same time periods, the SH ice area extents, which are minimally affected by land–sea transitions with sea level rise, are 20.9×10^6, 11.4×10^6, and 11.1×10^6 km^2, respectively.

During the 21 ka boreal winter, the Arctic Ocean and Baffin Bay are fully covered by ice and the ice around Greenland expands. The model displays increased sea ice in the western North Atlantic and decreased ice in the eastern North Atlantic and Nordic Seas, where the prescribed FIS margin advances into the water (Fig. 2). The limit of substantial coverage north of 55° N is in agreement with reconstructions (de Vernal et al., 2006) and other LGM simulations (Otto-Bliesner et al., 2006a; Roche et al., 2007); however, slight fractional cover (pack ice) in the model likely extends too far south (to $\sim 45°$ N) along the coast of North America. Fractional cover of up to 100 % is simulated in the far northwestern Pacific and the Sea of Okhotsk with a sharp, southward transition to reduced coverage. In boreal summer of the LGM, simulated sea ice retreats to 65° N in the North Atlantic and persists along eastern Canada, Baffin Bay and south of Greenland and the extreme northern areas of the Nordic Seas.

The overall distribution of SH sea ice (Fig. 11) is in good agreement with reconstructions and other model simulations (Gersonde et al., 2005; Roche et al., 2012). The simulated LGM maximum winter sea ice area is 35.5×10^6 km^2 (72 % greater than PI) and the LGM summer minimum is 4.8×10^6 km^2 (112 % greater than PI); the winter and summer reconstructed areas are $43.5 \pm 4 \times 10^6$ and $11.1 \pm 4 \times 10^6$ km^2, respectively (Roche et al., 2012). The seasonal amplitude (maximum minus minimum) of LGM ice cover simulated by GENMOM (30.6×10^6 km^2) is comparable with the reconstructed amplitude ($32.4 \pm 4 \times 10^6$ km^2) and the LGM-to-PI change of seasonality is well within the range simulated by the PMIP2 models (Roche et al., 2012, their Figs. 2 and 3).

3.5 Antarctic Circumpolar Current and Atlantic Meridional Overturning Circulation

The simulated ACC of 62 Sv is ∼ 48 % weaker than the observed value of 119 Sv through the Drake Passage (GECCO data; Köhl and Stammer, 2008). Although the T31 resolution of GENMOM is a factor in limiting flow through the Drake Passage, we attribute the underestimate of the ACC in part to insufficient wind stress at the latitude of the Drake Passage, which is caused by equatorward displacement of the core of the westerly winds, a shortcoming in common with other low-resolution AOGCMs (Alder et al., 2011; Russell et al., 2006; Schmittner et al., 2011a).

Considerable uncertainty exists in the proxies that are used to infer past changes in AMOC strength (Delworth and Zeng, 2008; Lynch-Stieglitz et al., 2007). The ^{231}Pa/^{230}Th record from 33° N on the Bermuda Rise (Lippold et al., 2009; McManus et al., 2004) indicates that, after the LGM, the strength of the AMOC began to diminish at ∼ 18 ka, was further reduced during Heinrich Event 1 (H1) at ∼ 17 ka, increased abruptly during the BA at 15 ka, and weakened again during the YD cold reversal at ∼ 12 ka. After the YD, the AMOC strengthened again and stabilized. In climate models, a variety of factors including the North Atlantic freshwater budget, model resolution, and parameterizations and the characteristics of simulated Antarctic Bottom Water (AABW) give rise to a considerable simulated range of AMOC (Weber et al., 2007).

The AMOC in our PI simulation (Fig. 12) is 19.3± 1.4 Sv at the core site of 33° N, a value similar to the present-day estimate of 18.7± 4.8 Sv at 26.5° N (Srokosz et al., 2012). The maximum AMOC simulated by GENMOM in the PI is 21.3 Sv at 41° N, a value outside the range of 13.8–20.8 Sv of five models in the PMIP2 experiments (Weber et al., 2007) but within the range of 3.8–31.7 Sv of the IPCC AR4 models (Meehl et al., 2007; Schmittner et al., 2005). The newer CMIP5 models have a narrower range of AMOC of ∼ 14 to ∼ 30 Sv when sampled at 30° N (Cheng et al., 2013); GENMOM simulates 16.0± 1.3 Sv at this location.

Our simulated LGM AMOC at the core site is 16.4 Sv, which is a ∼ 14.7 % reduction relative to the PI. The maximum LGM AMOC is 22.4 Sv at 40.8° N, an increase of 1.1 Sv (5.1 %) relative to the PI maximum and within the considerable range of −6.2 to +7.3 Sv in five PMIP2 simulations (Weber et al., 2007). In the deglacial simulations (21 through 15 ka), the northward (positive) AMOC flow extends deeper than that of the PI (Fig. 12) and the southward flow or AABW consequently is somewhat weakened. The maximum AMOC in GENMOM is essentially constant at the 40.8° N depth of 1.23 km for all time slices. Although the depth of the maximum is again comparable to the range of the PMIP2 models (1.24± 0.20), the invariance of the location and depth in GENMOM is likely a model-specific response.

Our time slice simulations display an increase in the strength of AMOC from the LGM to a maximum at 15 ka, decrease to a minimum at 9 ka, and remain more or less constant through the PI (Fig. 13), which is in apparent disagreement with the ^{231}Pa/^{230}Th records from which greater variability is inferred (Lippold et al., 2009; McManus et al., 2004). We do not expect to capture rapid and abrupt climate change events such as H1 (∼ 17 ka), the BA (∼ 15 ka), and the YD (∼ 12 ka) with only eight time slices, because we did not manipulate freshwater discharge to the North Atlantic in our experimental design.

4 21 and 6 ka data–model comparisons

We compare temperature and precipitation from our LGM and mid-Holocene simulations with paleoclimatic reconstructions and the PMIP3 simulations. For the LGM, we use the pollen-based reconstructions of mean annual mean temperature (MAT) and precipitation (MAP) from Bartlein et al. (2011) over land, as well as the Multiproxy Approach for the Reconstruction of the Glacial Ocean Surface (MARGO) project reconstructions over oceans (Waelbroeck et al., 2009). The gridded 2° × 2° pollen data include > 3000 terrestrial pollen records from Eurasia, Africa, and North America, and the global MARGO reconstruction comprises ∼ 700 analyses of planktonic foraminifera, diatom, dinoflagellate cyst and radiolarian abundances, alkenones, and planktonic foraminifera Mg / Ca from marine core sites. For 6 ka, we combine the pollen-based reconstructions of Bartlein et al. (2011) and the GHOST SST reconstructions (Leduc et al., 2010). The 6 ka GHOST data set contains ∼ 100 reconstructed temperature records based on analyses of alkenones and foraminifera Mg / Ca from marine sites located along continental margins and the Mediterranean Sea.

4.1 21 ka

Our simulated 21 ka anomalies of MAT and MAP are comparable with the pollen reconstructions (Fig. 14) and fall within the range of the PMIP3 models. GENMOM captures the mixed pattern of temperature and precipitation anomalies over Beringia that are present in the reconstructions (Fig. 14a, b) and in several of the PMIP3 simulations (Figs. S8, S9, and S16). The GENMOM SST anomalies indicate broad cooling of the global oceans (mean of −1.7 °C) but not as much cooling as is simulated in the PMIP3 models (mean of −2.9 °C); however, Harrison et al. (2013) found that the PMIP3 models tended to overestimate oceanic cooling. When sampled at the MARGO locations, GENMOM is generally warmer, but within the range of the PMIP3 models (Harrison et al., 2013). The overall agreement of the simulation with the MARGO data is good, but some features in the MARGO data are not reproduced by GENMOM. For example, similar to the PMIP3 simulations (Figs. S5, S6, and S16), the GENMOM simulation lacks the warming over the Greenland and Nordic Seas inferred from the data; however,

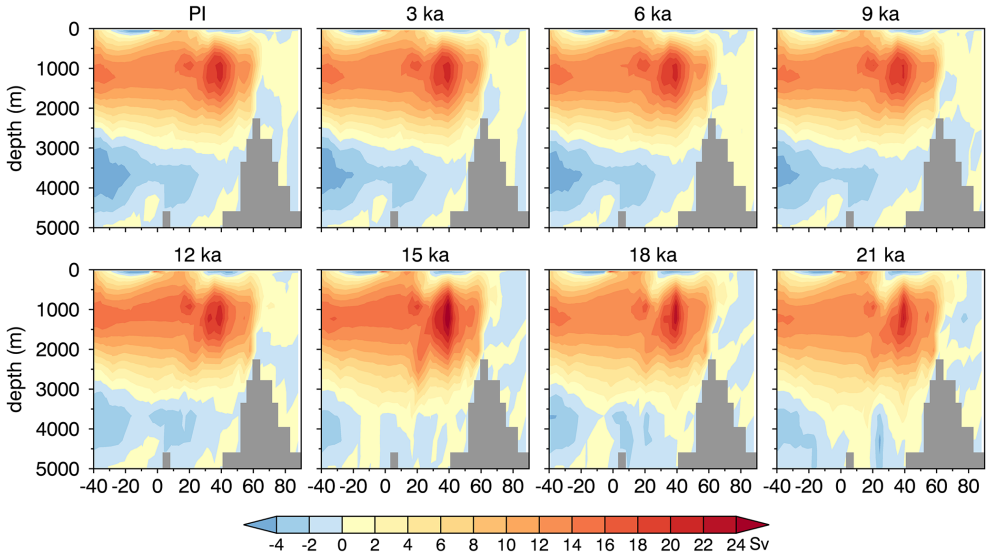

Figure 12. Simulated annual average Atlantic Meridional Overturning Circulation (AMOC) for the eight time slices.

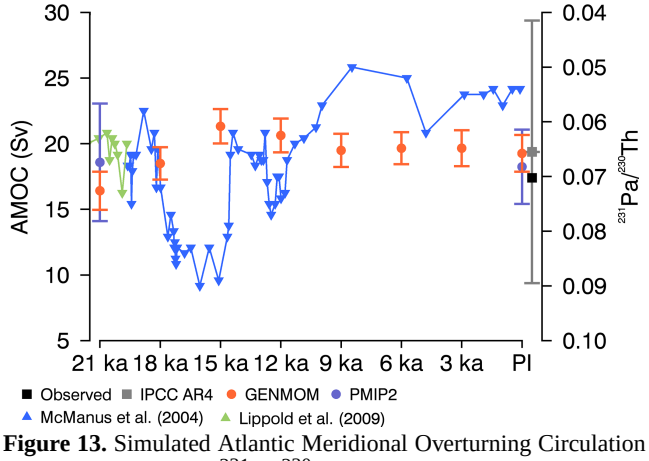

Figure 13. Simulated Atlantic Meridional Overturning Circulation (AMOC) compared to ^{231}Pa/^{230}Th proxy record at 33° N and other AOGCMs. Observations are from 26.5° N. GENMOM values are 100-year averages, with error bars representing standard deviations. The PMIP2 values represent the mean and standard deviation of the maximum AMOC from five models. The IPCC AR4 point represents the mean and standard deviation from a collection of IPCC AR4 models. ^{231}Pa/^{230}Th data from McManus et al. (2004) and Lippold et al. (2009), observed value from Srokosz et al. (2012), PMIP2 data from Weber et al. (2007), and IPCC data from Schmittner et al. (2005).

while the data indicate the Nordic Seas were ice-free at the LGM, the magnitude of the warming elsewhere, if it occurred, is somewhat unclear (de Vernal et al., 2006; Moller et al., 2013). The limited cooling along the western coast of North America and Mediterranean in GENMOM is attributed to the inability of the model to resolve the California Current and the Mediterranean circulation (Alder et al., 2011).

Over the tropical ocean basins, the 21 ka GENMOM simulation is 1.6 °C colder than the PI, in good agreement with the inferred MARGO cooling of 1.7± 1 °C (Otto-Bliesner et al., 2009). Average simulated SST anomalies are also similar to MARGO over the Indian (−1.6 °C versus −1.4 ± 0.7 °C) and Pacific (−1.5 °C versus −1.2 ± 1.1 °C) oceans but are warmer than the data in the tropical Atlantic basin (−1.9 °C versus −2.9±1.3 °C). In each of these regions, the anomalies simulated by GENMOM fall within the range of six PMIP2 models analyzed by Otto-Bliesner et al. (2009). GENMOM captures the 2–4 °C cooling in the eastern coastal Atlantic evident in the MARGO data, and the SST anomalies are ∼2–4 °C colder over the Western Pacific Warm Pool. Neither GENMOM nor the PMIP3 models reproduce the warming over the central and eastern tropics, low latitudes, and the North Atlantic evident in the MARGO reconstruction.

The simulated LGM MAP anomalies are also comparable with the pollen-based reconstructions (Fig. 14c and d). The model simulates general drying of the NH and a mix of increased and decreased precipitation in Beringia, South America, southern Africa, Southeast Asia, and Australia. GENMOM produces strong drying over and around the NH ice sheets, wetter-than-present conditions in the southwestern United States, and drying in Central America. The simulation fails to reproduce the drying over eastern North America that is inferred from the pollen-based data. There is considerable variability in the PMIP3 simulations of MAP (Figs. S9 and S10). In common with the PMIP3 models, GENMOM simulates a general reduction of precipitation over the NH, the North African and Indian monsoon regions, and Southeast Asia, as well as increased precipitation south of the LIS, southern Africa, and much of Australia (Fig. S16).

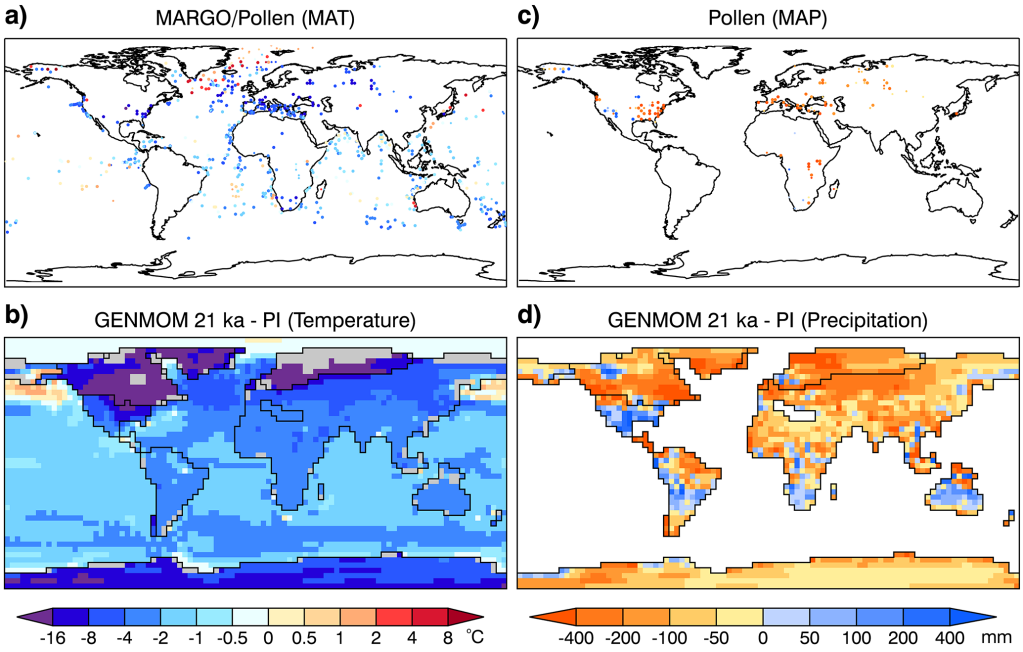

Figure 14. Changes in 21 ka mean annual temperature (MAT) and precipitation (MAP) inferred from data and simulated by GENMOM. **(a)** Blended sea surface temperature from MARGO (Waelbroeck et al., 2009) and terrestrial temperature from Bartlein et al. (2011), **(b)** GENMOM temperature anomalies (blended sea surface temperature and 2 m air temperature over land), **(c)** precipitation from Bartlein et al. (2011), and **(d)** GENMOM precipitation anomalies. Grid cells with different land mask types in the 21 ka and PI simulation are shaded in gray to avoid comparing ocean temperature to land temperature in emergent cells.

4.2 6 ka

Relative to PI, the changes in 6 ka boundary conditions are predominantly in the seasonality of insolation (Table 1) as opposed to the stronger radiative forcing associated with changes in GHGs and continental ice sheets from the LGM through the early Holocene. The resulting changes in 6 ka climatology are thus more subtle than those of the deglaciation. The changes of 6 ka MAT simulated by GENMOM are generally within the range of $\pm 1\,^{\circ}$C (Fig. 15b). Enhanced MAP and associated cooling are evident in the NH monsoonal regions (Fig. 15d). Elsewhere, MAP changes are within a range of ± 50 mm.

Pollen-based data reconstructions indicate highly heterogeneous changes in MAT during 6 ka; however, there are regions with spatially consistent changes in sign, such as warming south of Hudson Bay, areas of warming over Scandinavia and western Europe, and cooling in the Mediterranean region (Fig. 15a). Larger MAT changes at high-elevation sites and regions with anomalies of mixed sign occur in the data over most continents. The GENMOM 6 ka MAT anomalies also display a mix of warming and cooling in a range of about $\pm 4\,^{\circ}$C; however, where pollen-based records exist, the majority of the anomalies are within a narrower range of about $\pm 1.5\,^{\circ}$C (Fig. 15b). GENMOM, and many of the PMIP3 models (Figs. S8, S9, and S16), produces a mixture of warm and cold 6 ka MAT anomalies that are generally in the range of $\pm 1\,^{\circ}$C over the North Atlantic, Europe, and Scandinavia, which underestimates the proxy-based anomalies by $> 2\,^{\circ}$C at some sites.

The Asian pollen-based reconstruction similarly displays a heterogeneous temperature pattern that is reproduced by GENMOM and the PMIP3 models. In all of the models, the sign of the anomalies does not vary abruptly in close proximity to the pollen sites. We note, however, that the smooth topography in GCMs limits the ability of the models to reproduce large and regionally spatially heterogeneous anomalies that are characteristic of the local climate at many high-elevation pollen sites in western North America, the Alps, the central plateau of Africa, and Asia.

GENMOM displays cooling in the North African and Indian monsoon regions and warming over the high northern latitudes, consistent with the PMIP3 models (Fig. 15). In contrast, GENMOM simulates weak global cooling of $0.39\,^{\circ}$C compared to no change in the PMIP3 model average, which is partially attributed to our lower prescribed GHG concentrations (Table 1 caption).

Precipitation anomalies inferred from the pollen-based data indicate that 6 ka was wetter than the PI in Europe, Africa, Asia, and some parts of western North America and drier than PI in much of eastern North America and Scandinavia (Fig. 15c). GENMOM simulates the gradients and coherent patterns of positive and negative MAP anomalies over North America and northern, central, and western Africa, in

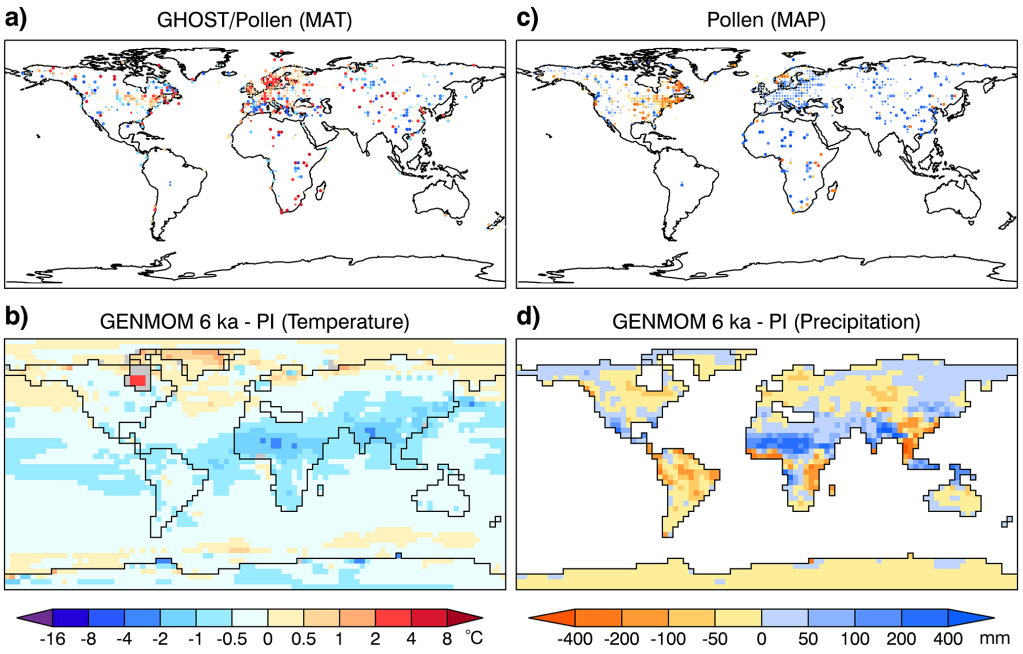

Figure 15. Changes in 6 ka mean annual temperature (MAT) and precipitation (MAP) inferred from data and simulated by GENMOM. **(a)** Blended sea surface temperature from Leduc et al. (2010) and terrestrial temperature from Bartlein et al. (2011), **(b)** GENMOM temperature anomalies (blended sea surface temperature and 2 m air temperature over land), **(c)** precipitation from Bartlein et al. (2011), and **(d)** GENMOM precipitation anomalies. Grid cells with different land mask types in the 6 ka and PI simulation are shaded in gray to avoid comparing ocean temperature to land temperature in emergent cells.

agreement with the data and the PMIP3 models. The data and GENMOM are also in agreement over the Asian monsoon region and northwestern Asia, where wetter conditions prevail, but anomalies of opposite sign are simulated over the Great Lowland Plain in north-central Eurasia and Southeast Asia. Bartlein et al. (2011) attribute cooling in Southeast Asia to a stronger winter monsoon at 6 ka. Our results (Figs. 6a and 8a), and many of the PMIP3 models, indicate cooler, drier winters (Figs. S7 and S11) and regionally variable changes in the summer (Figs. S8 and S12).

In Africa, the model captures the increase in precipitation in the northern and continental regions and drying along the southern coastal regions, as evident in the data. Strengthening of the African and Indian summer monsoons during the mid-Holocene corresponds well with the PMIP2 and PMIP3 models (Zheng and Braconnot, 2013). Both GENMOM and the data indicate drying over central Scandinavia, wetter conditions over east-central Europe, the Iberian Peninsula, and around the Mediterranean, but, over western Europe, the simulated decrease in MAP in GENMOM clearly disagrees with the data and some of the PMIP3 models (Figs. 15, S7, S8 and S16); however, the magnitude of the change in the models is very small and the sign of the change varies among models. Wetter conditions also prevail in Indonesia, and a southwest-to-northeast wet–dry gradient is simulated over Australia.

5 Summary

We have presented a suite of multi-century equilibrium climate simulations with GENMOM for the past 21 000 years at 3000-year intervals. Each 1100-year simulation was forced with fixed, time-appropriate global boundary conditions that included insolation, GHGs, continental ice sheets, and adjustment for sea level. The key drivers of climate change from the LGM through the Holocene are retreat of the NH ice sheets, increasing GHG concentrations, and latitudinal and seasonal variations in insolation.

GENMOM reasonably well reproduces the LGM to Holocene temperature trends inferred from the paleoclimate data syntheses of Shakun et al. (2012) and Marcott et al. (2013). The evolution of global temperature change simulated by GENMOM is consistent with three transient simulations, but is generally cooler during the deglacial time slices than the transient simulations when sampled at the proxy locations. The global LGM cooling of 3.8 °C simulated by GENMOM is within the range of 2.6–5.0 °C and average of 4.4 °C simulated by the PMIP3 models. Simulated LGM cooling of the tropical oceans is 1.6 °C, which is in good agreement with the MARGO reconstruction of 1.7 ± 1 °C. The weaker LGM global cooling is attributed to the sensitivity of GENMOM to CO_2 (2.2 °C for a 2× increase in the present-day value).

During the LGM, simulated precipitation is reduced globally by 8.2 % and gradually increases through the Holocene to present-day values in response to loss of the NH ice sheets, global warming, and related increases in atmospheric humidity. Between 15 and 6 ka seasonal changes in insolation altered the NH land–sea temperature contrasts, which, combined with shifts in global circulation, strengthened the summer monsoons in Africa and India. Monsoonal precipitation in both regions peaked between 12 and 9 ka, consistent with pollen-based reconstructions. The spatial patterns of mid-Holocene precipitation change simulated by GENMOM correspond well with the PMIP3 models, as do the 6 ka changes in monsoonal precipitation. In contrast to the pollen-based reconstructions, the GENMOM simulation shows western Europe to be slightly drier instead of slightly wetter than present.

The eight time slice simulations depict the glacial–interglacial transition that is in good agreement with other AOGCM simulations and compares reasonably well with data-based climate reconstructions. The data–model and model–model comparisons give us a measure of confidence that our paleo-GENMOM simulations are reasonable on broad spatial scales and add to the growing number of climate models that are capable of simulating key aspects of past climate change when constrained by a relatively small set of global boundary conditions. While our simulations are not continuous across the deglaciation and do not include events such as freshwater forcing, they do provide insights into between-period changes, such as altered NH storm tracks and strengthening of monsoons during the early to mid-Holocene and multi-century time series, that are useful, for example, to explore ecosystem responses to changes in mean climate and the related interannual variability in the model. Future work using the model output produced by this study will address how internal model variability and multidecadal variability influence comparison with proxy data, particularly North America, when using dynamical downscaling techniques.

Appendix A: List of abbreviations and acronyms.

AABW	Antarctic Bottom Water
ACC	Antarctic Circumpolar Current
AMOC	Atlantic Meridional Overturning Circulation
AOGCM	Atmosphere–ocean general circulation model
BA	Bølling–Allerød
CIS	Cordilleran Ice Sheet
CLIMAP	Climate: Long range Investigation, Mapping, and Prediction
COHMAP	Cooperative Holocene Mapping Project
DJF	December, January and February
FIS	Fennoscandian Ice Sheet
GECCO	German partner of Estimating the Circulation and Climate of the Ocean
GENESIS	Global Environmental and Ecological Simulation of Interactive Systems
GHG	Greenhouse gas
ITCZ	Intertropical Convergence Zone
H1	Heinrich Event 1
JJA	June, July, and August
LGM	Last Glacial Maximum
LIS	Laurentide Ice Sheet
LSX	Land Surface eXchange
MAM	March, April, and May
MAP	Mean annual precipitation
MARGO	Multiproxy Approach for the Reconstruction of the Glacial Ocean Surface Project
MAT	Mean annual temperature
MOM2	Modular Ocean Model version 2
NCAR	National Center for Atmospheric Research
NCEP	National Centers for Environmental Prediction
NH	Northern Hemisphere
OSU-LIS	Oregon State University Laurentide Ice Sheet
PD	Present day
PI	Preindustrial
PMIP	Paleoclimate Modelling Intercomparison Project
SH	Southern Hemisphere
SLP	Sea level pressure
SON	September, October, and November
SST	Sea surface temperature
TEMPO	Testing Earth System Models with Paleoenvironmental Observations
YD	Younger Dryas

The Supplement related to this article is available online at doi:10.5194/cp-11-449-2015-supplement.

Acknowledgements. We thank P. Bartlein, J. Shakun, S. Marcott, and the MARGO and GHOST project members for providing their proxy reconstructions. Z. Liu and J. Zhu kindly provided time series data for the three transient models CCSM3, LOVECLIM, and FAMOUS. We thank P. Bartlein, D. Pollard, and R. Thompson for their thoughtful reviews and A. Schmittner, S. Marcott, and P. Clark for helpful discussions and insights.

Edited by: M. Claussen

References

Alder, J. R., Hostetler, S. W., Pollard, D., and Schmittner, A.: Evaluation of a present-day climate simulation with a new coupled atmosphere-ocean model GENMOM, Geosci. Model Dev., 4, 69–83, doi:10.5194/gmd-4-69-2011, 2011.

Annan, J. D. and Hargreaves, J. C.: A new global reconstruction of temperature changes at the Last Glacial Maximum, Clim. Past, 9, 367–376, doi:10.5194/cp-9-367-2013, 2013.

Bartlein, P. J., Harrison, S. P., Brewer, S., Connor, S., Davis, B. A. S., Gajewski, K., Guiot, J., Harrison-Prentice, T. I., Henderson, A., Peyron, O., Prentice, I. C., Scholze, M., Seppä, H., Shuman, B., Sugita, S., Thompson, R. S., Viau, A. E., Williams, J., and Wu, H.: Pollen-based continental climate reconstructions at 6 and 21 ka: a global synthesis, Clim. Dynam., 37, 775–802, doi:10.1007/s00382-010-0904-1, 2011.

Beckmann, B., Flogel, S., Hofmann, P., Schulz, M., and Wagner, T.: Orbital forcing of Cretaceous river discharge in tropical Africa and ocean response, Nature, 437, 241–244, doi:10.1038/nature03976, 2005.

Berger, A. and Loutre, M. F.: Insolation values for the climate of the last 10 million years, Quaternary Sci. Rev., 10, 297–317, doi:10.1016/0277-3791(91)90033-Q, 1991.

Bice, K. L., Birgel, D., Meyers, P. A., Dahl, K. A., Hinrichs, K. U., and Norris, R. D.: A multiple proxy and model study of Cretaceous upper ocean temperatures and atmospheric CO_2 concentrations, Paleoceanography, 21, PA2002, doi:10.1029/2005PA001203, 2006.

Braconnot, P., Otto-Bliesner, B., Harrison, S., Joussaume, S., Peterchmitt, J.-Y., Abe-Ouchi, A., Crucifix, M., Driesschaert, E., Fichefet, Th., Hewitt, C. D., Kageyama, M., Kitoh, A., Laîné, A., Loutre, M.-F., Marti, O., Merkel, U., Ramstein, G., Valdes, P., Weber, S. L., Yu, Y., and Zhao, Y.: Results of PMIP2 coupled simulations of the Mid-Holocene and Last Glacial Maximum – Part 1: experiments and large-scale features, Clim. Past, 3, 261–277, doi:10.5194/cp-3-261-2007, 2007a.

Braconnot, P., Otto-Bliesner, B., Harrison, S., Joussaume, S., Peterchmitt, J.-Y., Abe-Ouchi, A., Crucifix, M., Driesschaert, E., Fichefet, Th., Hewitt, C. D., Kageyama, M., Kitoh, A., Loutre, M.-F., Marti, O., Merkel, U., Ramstein, G., Valdes, P., Weber, L., Yu, Y., and Zhao, Y.: Results of PMIP2 coupled simulations of the Mid-Holocene and Last Glacial Maximum – Part 2: feedbacks with emphasis on the location of the ITCZ and mid- and high latitudes heat budget, Clim. Past, 3, 279–296, doi:10.5194/cp-3-279-2007, 2007b.

Braconnot, P., Harrison, S. P., Kageyama, M., Bartlein, P. J., Masson-Delmotte, V., Abe-Ouchi, A., Otto-Bliesner, B. L., and Zhao, Y.: Evaluation of climate models using palaeoclimatic data, Nat. Geosci., 2, 417–424, doi:10.1038/nclimate1456, 2012.

Broccoli, A. J., Dahl, K. A., and Stouffer, R. J.: Response of the ITCZ to Northern Hemisphere cooling, Geophys. Res. Lett., 33, L01702, doi:10.1029/2005GL024546, 2006.

Brohan, P., Kennedy, J. J., Harris, I., Tett, S. F. B., and Jones, P. D.: Uncertainty estimates in regional and global observed temperature changes: a new data set from 1850, J. Geophys. Res., 111, D12106, doi:10.1029/2005JD006548, 2006.

Brook, E. J., Harder, S., Severinghaus, J., Steig, E. J., and Sucher, C. M.: On the origin and timing of rapid changes in atmospheric methane during the last glacial period, Global Biogeochem. Cy., 14, 559–572, 2000.

Cheng, H., Sinha, A., Wang, X., Cruz, F. W., and Edwards, R. L.: The Global Paleomonsoon as seen through speleothem records from Asia and the Americas, Clim. Dynam., 39, 1045–1062, doi:10.1007/s00382-012-1363-7, 2012.

Cheng, W., Chiang, J. C. H., and Zhang, D.: Atlantic Meridional Overturning Circulation (AMOC) in CMIP5 Models: RCP and Historical Simulations, J. Climate, 26, 7187–7197, doi:10.1175/JCLI-D-12-00496.1, 2013.

Chiang, J. C. H.: The Tropics in Paleoclimate, Annu. Rev. Earth Pl. Sc., 37, 263–297, doi:10.1146/annurev.earth.031208.100217, 2009.

Chiang, J. C. H. and Bitz, C. M.: Influence of high latitude ice cover on the marine Intertropical Convergence Zone, Clim. Dynam., 25, 477–496, doi:10.1007/s00382-005-0040-5, 2005.

Clark, P. U., Shakun, J. D., Baker, P. A., Bartlein, P. J., Brewer, S., Brook, E., Carlson, A. E., Cheng, H., Kaufman, D. S., Liu, Z. Y., Marchitto, T. M., Mix, A. C., Morrill, C., Otto-Bliesner, B. L., Pahnke, K., Russell, J. M., Whitlock, C., Adkins, J. F., Blois, J. L., Clark, J., Colman, S. M., Curry, W. B., Flower, B. P., He, F., Johnson, T. C., Lynch-Stieglitz, J., Markgraf, V., McManus, J., Mitrovica, J. X., Moreno, P. I., and Williams, J. W.: Global climate evolution during the last deglaciation, P. Natl. Acad. Sci. USA, 109, E1134–E1142, doi:10.1073/Pnas.1116619109, 2012.

Claussen, M.: Late Quaternary vegetation-climate feedbacks, Clim. Past, 5, 203–216, doi:10.5194/cp-5-203-2009, 2009.

CLIMAP Project Members: Seasonal reconstructions of the earth's surface at the Last Glacial Maximum, Geological Society of America, Map and Chart Series, MC-36, 1981.

COHMAP Members: Climatic Changes of the Last 18,000 Years: Observations and Model Simulations, Science, 241, 1043–1052, 1988.

DeConto, R. M., Pollard, D., and Harwood, D.: Sea ice feedback and Cenozoic evolution of Antarctic climate and ice sheets, Paleoceanography, 22, PA3214, doi:10.1029/2006PA001350, 2007.

DeConto, R. M., Pollard, D., Wilson, P. A., Palike, H., Lear, C. H., and Pagani, M.: Thresholds for Cenozoic bipolar glaciation, Nat. Geosci., 455, 652–656, doi:10.1038/nature07337, 2008.

Delworth, T. L. and Zeng, F.: Simulated impact of altered Southern Hemisphere winds on the Atlantic meridional overturning circulation, Geophys. Res. Lett., 35, L20708, doi:10.1029/2008gl035166, 2008.

de Vernal, A., Rosell-Mele, A., Kucera, M., Hillaire-Marcel, C., Eynaud, F., Weinelt, M., Dokken, T., and Kageyama, M.: Comparing proxies for the reconstruction of LGM sea-surface conditions in the northern North Atlantic, Quaternary Sci. Rev., 25, 2820–2834, doi:10.1016/j.quascirev.2006.06.006, 2006.

DiNezio, P. N. and Tierney, J. E.: The effect of sea level on glacial Indo-Pacific climate, Nat. Geosci., 6, 1–7, doi:10.1038/ngeo1823, 2013.

Dorman, J. L. and Sellers, P. J.: A global climatology of albedo, roughness length and stomatal-resistance for atmospheric general-circulation models as represented by the simple biosphere model (Sib), J. Appl. Meteorol., 28, 833–855, doi:10.1175/1520-0450(1989)028<0833:Agcoar>2.0.Co;2, 1989.

Dyke, A. S. and Prest, V. K.: Late Wisconsinan and Holocene History of the Laurentide Ice Sheet, Geogr. Phys. Quatern., 41, 237–263, 1987.

Felzer, B.: Climate impacts of an ice sheet in East Siberia during the Last Glacial Maximum, Quaternary Sci. Rev., 20, 437–447, doi:10.1016/S0277-3791(00)00106-2, 2001.

Felzer, B., Oglesby, R. J., Webb, T., and Hyman, D. E.: Sensitivity of a general circulation model to changes in Northern Hemisphere ice sheets, J.-Geophys.-Res., 101, 19077–19092, 1996.

Felzer, B., Webb, T., and Oglesby, R. J.: The impact of ice sheets, CO_2, and orbital insolation on late quaternary climates: sensitivity experiments with a general circulation model, Quaternary Sci. Rev., 17, 507–534, doi:10.1016/S0277-3791(98)00010-9, 1998.

Flato, G. M. and Hibler, W. D.: Modeling Pack Ice as a Cavitating Fluid, J. Phys. Oceanogr., 22, 626–651, 1992.

Gasse, F.: Hydrological changes in the African tropics since the Last Glacial Maximum, Quaternary Sci. Rev., 19, 189–211, doi:10.1016/S0277-3791(99)00061-X, 2000.

Gates, W. L. and Nelson, A. B.: A new (revised) tabulation of the Scripps topography on a 1 degree global grid, Part 1: Terrain heights, Tech. Rep. R-1276-1-ARPA, The Rand Corporation, Santa Monica, CA, 132 pp., 1975.

Gent, P. R. and McWilliams, J. C.: Isopycnal mixing in ocean circulation models, J. Phys. Oceanogr., 20, 150–155, doi:10.1175/1520-0485(1990)020<0150:IMIOCM>2.0.CO;2, 1990.

Gersonde, R., Crosta, X., Abelmann, A., and Armand, L.: Sea-surface temperature and sea ice distribution of the Southern Ocean at the EPILOG Last Glacial Maximum – a circum-Antarctic view based on siliceous microfossil records, Quaternary Sci. Rev., 24, 869–896, doi:10.1016/j.quascirev.2004.07.015, 2005.

Harrison, S. P., Bartlein, P. J., Brewer, S., Prentice, I. C., Boyd, M., Hessler, I., Holmgren, K., Izumi, K., and Willis, K.: Climate model benchmarking with glacial and mid-Holocene climates, Clim. Dynam., 1–18, doi:10.1007/s00382-013-1922-6, 2013.

Harvey, L. D. D.: Development of a Sea Ice Model for Use in Zonally Averaged Energy Balance Climate Models, J. Climate, 1, 1221–1238, 1988.

Hassol, S. J.: Impacts of a Warming Arctic – Arctic Climate Impact Assessment, Arctic Climate Impact Assessment, ISBN 0521617782, Cambridge University Press, Cambridge, UK, 144 pp., 2004.

Hély, C., Braconnot, P., Watrin, J., and Zheng, W.: Climate and vegetation: simulating the African humid period, CR Geosci., 341, 671–688, doi:10.1016/j.crte.2009.07.002, 2009.

Horton, D. E., Poulsen, C. J., and Pollard, D.: Orbital and CO_2 forcing of late Paleozoic continental ice sheets, Geophys. Res. Lett., 34, L19708, doi:10.1029/2007GL031188, 2007.

Hostetler, S. W., Clark, P. U., Bartlein, P. J., Mix, A. C., and Pisias, N. J.: Atmospheric transmission of North Atlantic Heinrich events, J. Geophys. Res., 104, 3947–3952, 1999.

Hostetler, S. W., Pisias, N., and Mix, A. C.: Sensitivity of Last Glacial Maximum climate to uncertainties in tropical and subtropical ocean temperatures, Quaternary Sci. Rev., 25, 1168–1185, doi:10.1016/j.quascirev.2005.12.010, 2006.

Jaccard, S. L., Haug, G. H., Sigman, D. M., Pedersen, T. F., Thierstein, H. R., and Rohl, U.: Glacial/interglacial changes in subarctic North Pacific stratification, Science, 308, 1003–1006, doi:10.1126/science.1108696, 2005.

Joussaume, S., Taylor, K. E., Braconnot, P., Mitchell, J., Kutzbach, J. E., Harrison, S. P., Prentice, I. C., Broccoli, A. J., Abe-Ouchi, A., Bartlein, P. J., Bonfils, C., Dong, B., Guiot, J., Herterich, K., Hewitt, C. D., Jolly, D., Kim, J. W., Kislov, A., Kitoh, A., Loutre, M. F., Masson, V., McAvaney, B., McFarlane, N., de Noblet, N., Peltier, W. R., Peterschmitt, J. Y., Pollard, D., Rind, D., Royer, J. F., Schlesinger, M. E., Syktus, J., Thompson, S. L., Valdes, P., Vettoretti, G., Webb, R. S., and Wyputta, U.: Monsoon changes for 6000 years ago: results of 18 simulations from the Paleoclimate Modeling Intercomparison Project (PMIP), Geophys. Res. Lett., 26, 859–862, 1999.

Kageyama, M., D'Andrea, F., Ramstein, G., Valdes, P. J., and Vautard, R.: Weather regimes in past climate atmospheric general circulation model simulations, Clim. Dynam., 15, 773–793, doi:10.1007/S003820050315, 1999.

Kageyama, M., Laîné, A., Abe-Ouchi, A., Braconnot, P., Cortijo, E., Crucifix, M., de Vernal, A., Guiot, J., Hewitt, C. D., and Kitoh, A.: Last Glacial Maximum temperatures over the North Atlantic, Europe and western Siberia: a comparison between PMIP models, MARGO sea–surface temperatures and pollen-based reconstructions, Quaternary Sci. Rev., 25, 2082–2102, doi:10.1016/j.quascirev.2006.02.010, 2006.

Kalnay, E., Kanamitsu, M., Kistler, R., Collins, W., Deaven, D., Gandin, L., Iredell, M., Saha, S., White, G., Woollen, J., Zhu, Y., Chelliah, M., Ebisuzaki, W., Higgins, W., Janowiak, J., Mo, K. C., Ropelewski, C., Wang, J., Leetmaa, A., Reynolds, R., Jenne, R., and Joseph, D.: The NCEP/NCAR 40 year reanalysis project, B. Am. Meteorol. Soc., 77, 437–471, 1996.

Kiehl, J. T., Hack, J. J., Bonan, G. B., Boville, B. A., Williamson, D. L., and Rasch, P. J.: The National Center for Atmospheric Research Community Climate Model: CCM3, J. Climate, 11, 1131–1149, 1998.

Kim, S.-J., Crowley, T. J., Erickson, D. J., Govindasamy, B., Duffy, P. B., and Lee, B. Y.: High-resolution climate simulation of the last glacial maximum, Clim. Dynam., 31, 1–16, doi:10.1007/s00382-007-0332-z, 2007.

Köhl, A. and Stammer, D.: Decadal sea level changes in the 50 year GECCO ocean synthesis, J. Climate, 21, 1876–1890, doi:10.1175/2007JCLI2081.1, 2008.

Köhler, P., Bintanja, R., Fischer, H., Joos, F., Knutti, R., Lohmann, G., and Masson-Delmotte, V.: What caused Earth's temperature variations during the last 800,000 years?

Data-based evidence on radiative forcing and constraints on climate sensitivity, Quaternary Sci. Rev., 29, 129–145, doi:10.1016/j.quascirev.2009.09.026, 2010.

Kump, L. R. and Pollard, D.: Amplification of cretaceous warmth by biological cloud feedbacks, Science, 320, 195–195, doi:10.1126/science.1153883, 2008.

Kutzbach, J. E. and Liu, Z.: Response of the African Monsoon to orbital forcing and ocean feedbacks in the middle holocene, Science, 278, 440–443, doi:10.1126/science.278.5337.440, 1997.

Kutzbach, J. E. and Otto-Bliesner, B. L.: The sensitivity of the African–Asian monsoonal climate to orbital parameter changes for 9000 years BP in a low-resolution general-circulation model, J. Atmos. Sci., 39, 1177–1188, 1982.

Kutzbach, J. E., Bartlein, P. J., FOLEY, J. A., Harrison, S. P., Hostetler, S. W., Liu, Z., Prentice, I. C., and WEBB, T. I.: Potential role of vegetation feedback in the climate sensitivity of high-latitude regions: A case study at 6000 years B.P., Global Biogeochem. Cy., 10, 727–736, 1996a.

Kutzbach, J., Bonan, G., Foley, J., and Harrison, S. P.: Vegetation and soil feedbacks on the response of the African monsoon to orbital forcing in the early to middle Holocene, Nature, 384, 623–626, doi:10.1038/384623a0, 1996b.

Kutzbach, J., Gallimore, R., Harrison, S., Behling, P., Selin, R., and Laarif, F.: Climate and biome simulations for the past 21,000 years, Quaternary Sci. Rev., 17, 473–506, 1998.

Leduc, G., Schneider, R., Kim, J. H., and Lohmann, G.: Holocene and Eemian sea surface temperature trends as revealed by alkenone and Mg / Ca paleothermometry, Quaternary Sci. Rev., 29, 989–1004, doi:10.1016/j.quascirev.2010.01.004, 2010.

Lee, J.-Y., and Wang, B.: Future change of global monsoon in the CMIP5, Clim. Dynam., 42, 101–119, doi:10.1007/s00382-012-1564-0, 2014.

Li, C. and Battisti, D. S.: Reduced Atlantic storminess during Last Glacial Maximum: evidence from a coupled climate model, J. Climate, 21, 3561–3579, doi:10.1175/2007jcli2166.1, 2008.

Licciardi, J. M., Clark, P. U., Jenson, J. W., and Macayeal, D. R.: Deglaciation of a soft-bedded Laurentide ice sheet, Quaternary Sci. Rev., 17, 427–448, doi:10.1016/S0277-3791(97)00044-9, 1998.

Lippold, J., Grützner, J., Winter, D., Lahaye, Y., Mangini, A., and Christl, M.: Does sedimentary $^{231}Pa/^{230}Th$ from the Bermuda rise monitor past Atlantic meridional overturning circulation? Geophys. Res. Lett., 36, L12601, doi:10.1029/2009gl038068, 2009.

Liu, Z., Otto-Bliesner, B. L., He, F., Brady, E. C., Tomas, R., Clark, P. U., Carlson, A. E., Lynch-Stieglitz, J., Curry, W., Brook, E., Erickson, D., Jacob, R., Kutzbach, J., and Cheng, J.: Transient simulation of last deglaciation with a new mechanism for Bolling–Allerod warming, Science, 325, 310–314, doi:10.1126/science.1171041, 2009.

Liu, Z., Zhu, J., Rosenthal, Y., Zhang, X., Otto-Bliesner, B. L., Timmermann, A., Smith, R. S., Lohmann, G., Zheng, W., and Elison Timm, O.: The Holocene temperature conundrum, P. Natl. Acad. Sci. USA, 111, E3501–E3505, doi:10.1073/pnas.1407229111, 2014.

Lynch-Stieglitz, J., Adkins, J. F., Curry, W. B., Dokken, T., Hall, I. R., Herguera, J. C., Hirschi, J. J., Ivanova, E. V., Kissel, C., Marchal, O., Marchitto, T. M., McCave, I. N., McManus, J. F., Mulitza, S., Ninnemann, U., Peeters, F., Yu, E. F., and Zahn, R.: Atlantic meridional overturning circulation during the Last Glacial Maximum, Science, 316, 66–69, doi:10.1126/science.1137127, 2007.

Marcott, S. A., Shakun, J. D., Clark, P. U., and Mix, A. C.: A Reconstruction of Regional and Global Temperature for the Past 11,300 Years, Science, 339, 1198–1201, doi:10.1126/Science.1228026, 2013.

Marzin, C. and Braconnot, P.: Variations of Indian and African monsoons induced by insolation changes at 6 and 9.5 kyr BP, Clim. Dynam., 33, 215–231, doi:10.1007/s00382-009-0538-3, 2009.

McManus, J. F., Francois, R., Gherardi, J. M., Keigwin, L. D., and Brown-Leger, S.: Collapse and rapid resumption of Atlantic meridional circulation linked to deglacial climate changes, Nature, 428, 834–837, doi:10.1038/Nature02494, 2004.

Meehl, G. A., Stocker, T. F., and Collins, W. D.: Global climate projections, in: Climate Change 2007: The Physical Science Basis. Contribution of Working Group I to the Fourth Assessment Report of the Intergovernmental Panel on Climate Change, edited by: Solomon, S., Qin, D., Manning, M., Chen, Z., Marquis, M., Averyt, K. B., Tignor, M., and Miller, H. L., Cambridge University Press, Cambridge, UK and New York, NY, USA, 2007.

Miller, G., Mangan, J., Pollard, D., Thompson, S. L., Felzer, B., and Magee, J.: Sensitivity of the Australian Monsoon to insolation and vegetation: implications for human impact on continental moisture balance, Geology, 33, 65–68, 2005.

Moller, T., Schulz, H., and Kucera, M.: The effect of sea surface properties on shell morphology and size of the planktonic foraminifer Neogloboquadrina pachyderma in the North Atlantic, Palaeogeogr. Palaeocl., 391, 34–48, doi:10.1016/j.palaeo.2011.08.014, 2013.

Monnin, E., Indermuhle, A., Dallenbach, A., Fluckiger, J., Stauffer, B., Stocker, T. F., Raynaud, D., and Barnola, J. M.: Atmospheric CO_2 concentrations over the last glacial termination, Science, 291, 112–114, 2001.

Otto-Bliesner, B. L., Brady, E. C., Clauzet, G., Tomas, R., Levis, S., and Kothavala, Z.: Last Glacial Maximum and Holocene climate in CCSM3, J. Climate, 19, 2526–2544, doi:10.1175/Jcli3748.1, 2006a.

Otto-Bliesner, B. L., Tomas, R., Brady, E. C., Ammann, C., Kothavala, Z., and Clauzet, G.: Climate sensitivity of moderate- and low-resolution versions of CCSM3 to preindustrial forcings, J. Climate, 19, 2567–2583, doi:10.1175/Jcli3754.1, 2006b.

Otto-Bliesner, B. L., Schneider, R., Brady, E. C., Kucera, M., Abe-Ouchi, A., Bard, E., Braconnot, P., Crucifix, M., Hewitt, C. D., Kageyama, M., Marti, O., Paul, A., Rosell-Mele, A., Waelbroeck, C., Weber, S. L., Weinelt, M., and Yu, Y.: A comparison of PMIP2 model simulations and the MARGO proxy reconstruction for tropical sea surface temperatures at last glacial maximum, Clim. Dynam., 32, 799–815, doi:10.1007/s00382-008-0509-0, 2009.

Pacanowski, R. C.: MOM 2 Version 2.0 (Beta) Documentation: User's Guide and Reference Manual, Technical Report 3.2, NOAA GFDL Ocean Group, GFDL, Princeton, New Jersey, 329 pp., 1996.

Pausata, F. S. R., Li, C., Wettstein, J.'J., Kageyama, M., and Nisancioglu, K. H.: The key role of topography in altering North Atlantic atmospheric circulation during the last glacial period, Clim. Past, 7, 1089–1101, doi:10.5194/cp-7-1089-2011, 2011.

Peixoto, J. P. and Oort, A. H.: The Physics of Climate, 3rd Edn., American Institute of Physics, New York, 1992.

Peltier, W. R.: Global glacial isostatic adjustment: palaeogeodetic and space-geodetic tests of the ICE-4G (VM2) model, J. Quaternary Sci., 17, 491–510, doi:10.1002/jqs.713, 2002.

Pinot, S., Ramstein, G., Harrison, S. P., Prentice, I. C., Guiot, J., Stute, M., and Joussaume, S.: Tropical paleoclimates at the Last Glacial Maximum: comparison of Paleoclimate Modeling Intercomparison Project (PMIP) simulations and paleodata, Clim. Dynam., 15, 857–874, 1999.

Pollard, D. and Reusch, D. B.: A calendar conversion method for monthly mean paleoclimate model output with orbital forcing, J. Geophys. Res., 107, 4615, doi:10.1029/2002JD002126, 2002.

Pollard, D. and Thompson, S. L.: Sea-ice dynamics and CO_2 sensitivity in a global climate model, Atmos. Ocean, 32, 449–467, doi:10.1080/07055900.1994.9649506, 1994.

Pollard, D. and Thompson, S. L.: Use of a Land-Surface-Transfer Scheme (Lsx) in a global climate model – the response to doubling stomatal-resistance, Global Planet. Change, 10, 129–161, doi:10.1016/0921-8181(94)00023-7, 1995.

Pollard, D. and Thompson, S. L.: Climate and ice-sheet mass balance at the last glacial maximum from the genesis version 2 global climate model, Quaternary Sci. Rev., 16, 841–863, 1997.

Pollard, D., Bergengren, J. C., Stillwell-Soller, L. M., Felzer, B., and Thompson, S. L.: Climate simulations for 10 000 and 6000 years BP using the GENESIS global climate model, Palaeoclimates: Data and Modelling, 2, 183–218, 1998.

Poulsen, C. J., Pollard, D., and White, T. S.: General circulation model simulation of the delta O-18 content of continental precipitation in the middle Cretaceous: a model-proxy comparison, Geology, 35, 199–202, doi:10.1130/G23343A.1, 2007a.

Poulsen, C. J., Pollard, D., Montanez, I. P., and Rowley, D.: Late Paleozoic tropical climate response to Gondwanan deglaciation, Geology, 35, 771–774, doi:10.1130/G23841A.1, 2007b.

Ramstein, G. and Joussaume, S.: Sensitivity experiments to sea surface temperatures, sea-ice extent and ice-sheet reconstruction for the Last Glacial Maximum, Ann. Glaciol., 21, 343–347, 1995.

Renssen, H., Goosse, H., Fichefet, T., Brovkin, V., Driesschaert, E., and Wolk, F.: Simulating the Holocene climate evolution at northern high latitudes using a coupled atmosphere-sea ice-ocean-vegetation model, Clim. Dynam., 24, 23–43, doi:10.1007/s00382-004-0485-y, 2004.

Rind, D.: Components of the Ice-Age circulation, J. Geophys. Res., 92, 4241–4281, 1987.

Roche, D. M., Dokken, T. M., Goosse, H., Renssen, H., and Weber, S. L.: Climate of the Last Glacial Maximum: sensitivity studies and model-data comparison with the LOVECLIM coupled model, Clim. Past, 3, 205–224, doi:10.5194/cp-3-205-2007, 2007.

Roche, D. M., Crosta, X., and Renssen, H.: Evaluating Southern Ocean sea-ice for the Last Glacial Maximum and pre-industrial climates: PMIP-2 models and data evidence, Quaternary Sci. Rev., 56, 99–106, doi:10.1016/j.quascirev.2012.09.020, 2012.

Rohling, E. J., Medina-Elizalde, M., Shepherd, J. G., Siddall, M., and Stanford, J. D.: Sea Surface and High-Latitude Temperature Sensitivity to Radiative Forcing of Climate over Several Glacial Cycles, J. Climate, 25, 1635–1656, doi:10.1175/2011JCLI4078.1, 2012.

Ruddiman, W. F., Vavrus, S. J., and Kutzbach, J. E.: A test of the overdue-glaciation hypothesis, Quaternary Sci. Rev., 24, 1–10, doi:10.1016/j.quascirev.2004.07.010, 2005.

Russell, J. L., Stouffer, R. J., and Dixon, K. W.: Intercomparison of the Southern Ocean circulations in IPCC coupled model control simulations, J. Climate, 19, 4560–4575, doi:10.1175/Jcli3869.1, 2006.

Schmittner, A., Latif, M., and Schneider, B.: Model projections of the North Atlantic thermohaline circulation for the 21st century assessed by observations, Geophys. Res. Lett., 32, L23710, doi:10.1029/2005gl024368, 2005.

Schmittner, A., Silva, T. A. M., Fraedrich, K., Kirk, E., and Lunkeit, F.: Effects of mountains and ice sheets on Global Ocean Circulation, J. Climate, 24, 2814–2829, doi:10.1175/2010jcli3982.1, 2011a.

Schmittner, A., Urban, N. M., Shakun, J. D., Mahowald, N. M., Clark, P. U., Bartlein, P. J., Mix, A. C., and Rosell-Mele, A.: Climate sensitivity estimated from temperature reconstructions of the Last Glacial Maximum, Science, 334, 1385–1388, doi:10.1126/science.1203513, 2011b.

Semtner Jr., A. J.: A model for the thermodynamic growth of sea ice in numerical investigations of climate, J. Phys. Oceanogr., 6, 379–389, doi:10.1175/1520-0485(1976)006<0379:AMFTTG>2.0.CO;2, 1976.

Shakun, J. D., Clark, P. U., He, F., Marcott, S. A., Mix, A. C., Liu, Z., Otto-Bliesner, B. L., Schmittner, A., and Bard, E.: Global warming preceded by increasing carbon dioxide concentrations during the last deglaciation, Nature, 484, 49–54, doi:10.1038/nature10915, 2012.

Singarayer, J. S. and Valdes, P. J.: High-latitude climate sensitivity to ice-sheet forcing over the last 120 kyr, Quaternary Sci. Rev., 29, 43–55, doi:10.1016/j.quascirev.2009.10.011, 2010.

Smith, R. S. and Gregory, J.: The last glacial cycle: transient simulations with an AOGCM, Clim. Dynam., 38, 1545–1559, doi:10.1007/s00382-011-1283-y, 2012.

Sowers, T., Alley, R. B., and Jubenville, J.: Ice Core Records of Atmospheric N_2O Covering the Last 106,000 Years, Science, 301, 945–948, doi:10.1126/science.1085293, 2003.

Srokosz, M., Baringer, M., Bryden, H., Cunningham, S., Delworth, T., Lozier, S., Marotzke, J., and Sutton, R.: Past, present, and future changes in the atlantic meridional overturning circulation, B. Am. Meteorol. Soc., 93, 1663–1676, doi:10.1175/bams-d-11-00151.1, 2012.

Tabor, C. R., Poulsen, C. J., and Pollard, D.: Mending Milankovitch's theory: obliquity amplification by surface feedbacks, Clim. Past, 10, 41–50, doi:10.5194/cp-10-41-2014, 2014.

Thompson, S. L. and Pollard, D.: A Global Climate Model (GENESIS) with a Land-Surface Transfer Scheme (LSX). Part I: Present Climate Simulation, J. Climate, 8, 732–761, 1995.

Thompson, S. L. and Pollard, D.: Greenland and Antarctic mass balances for present and doubled atmospheric CO_2 from the GENESIS version-2 global climate model, J. Climate, 10, 871–900, 1997.

Timm, O. and Timmermann, A.: Simulation of the Last 21 000 Years Using Accelerated Transient Boundary Conditions, J. Climate, 20, 4377–4401, doi:10.1175/JCLI4237.1, 2007.

Timm, O., Timmermann, A., Abe-Ouchi, A., Saito, F., and Segawa, T.: On the definition of seasons in paleoclimate simulations with orbital forcing, Paleoceanography, 23, PA2221, doi:10.1029/2007PA001461, 2008.

Timm, O., Köhler, P., Timmermann, A., and Menviel, L.: Mechanisms for the onset of the African humid period and Sahara greening 14.5–11 ka BP, J. Climate, 23, 2612–2633, doi:10.1175/2010jcli3217.1, 2010.

Ullman, D. J., LeGrande, A. N., Carlson, A. E., Anslow, F. S., and Licciardi, J. M.: Assessing the impact of Laurentide Ice Sheet topography on glacial climate, Clim. Past, 10, 487–507, doi:10.5194/cp-10-487-2014, 2014.

Unterman, M. B., Crowley, T. J., Hodges, K. I., Kim, S. J., and Erickson, D. J.: Paleometeorology: high resolution Northern Hemisphere wintertime mid-latitude dynamics during the Last Glacial Maximum, Geophys. Res. Lett., 38, L23702, doi:10.1029/2011gl049599, 2011.

Waelbroeck, C., Paul, A., Kucera, M., Rosell-Mele, A., Weinelt, M., Schneider, R., Mix, A. C., Abelmann, A., Armand, L., Bard, E., Barker, S., Barrows, T. T., Benway, H., Cacho, I., Chen, M. T., Cortijo, E., Crosta, X., de Vernal, A., Dokken, T., Duprat, J., Elderfield, H., Eynaud, F., Gersonde, R., Hayes, A., Henry, M., Hillaire-Marcel, C., Huang, C. C., Jansen, E., Juggins, S., Kallel, N., Kiefer, T., Kienast, M., Labeyrie, L., Leclaire, H., Londeix, L., Mangin, S., Matthiessen, J., Marret, F., Meland, M., Morey, A. E., Mulitza, S., Pflaumann, U., Pisias, N. G., Radi, T., Rochon, A., Rohling, E. J., Sbaffi, L., Schaefer-Neth, C., Solignac, S., Spero, H., Tachikawa, K., Turon, J. L., and Members, M. P.: Constraints on the magnitude and patterns of ocean cooling at the Last Glacial Maximum, Nat. Geosci., 2, 127–132, doi:10.1038/NGEO411, 2009.

Weber, S. L., Drijfhout, S. S., Abe-Ouchi, A., Crucifix, M., Eby, M., Ganopolski, A., Murakami, S., Otto-Bliesner, B., and Peltier, W. R.: The modern and glacial overturning circulation in the Atlantic ocean in PMIP coupled model simulations, Clim. Past, 3, 51–64, doi:10.5194/cp-3-51-2007, 2007.

Zhao, Y. and Harrison, S. P.: Mid-Holocene monsoons: a multi-model analysis of the inter-hemispheric differences in the responses to orbital forcing and ocean feedbacks, Clim. Dynam., 39, 1457–1487, doi:10.1007/s00382-011-1193-z, 2012.

Zheng, W. and Braconnot, P.: Characterization of model spread in PMIP2 mid-holocene simulations of the African monsoon, J. Climate, 26, 1192–1210, doi:10.1175/JCLI-D-12-00071.1, 2013.

Zhou, J., Poulsen, C. J., Pollard, D., and White, T. S.: Simulation of modern and middle Cretaceous marine delta δ^{18}O with an ocean–atmosphere general circulation model, Paleoceanography, 23, PA3223, doi:10.1029/2008pa001596, 2008.